

1 *Research article*

## 2 **Automated riverbed material analysis using Deep Learning on** 3 **underwater images**

4 Alexander A. Ermilov<sup>1</sup>, Gergely Benkő<sup>1</sup> and Sándor Baranya<sup>1</sup>

5 <sup>1</sup>Department of Hydraulic and Water Resources Engineering, Budapest University of Technology and Economics,  
6 Budapest, 1111, Hungary

7 *Correspondence to:* Alexander A. Ermilov ([ermilov.alexander@emk.bme.hu](mailto:ermilov.alexander@emk.bme.hu))

8 **Abstract.** The sediment of alluvial riverbeds plays a significant role in river systems both in engineering and  
9 natural processes. However, the sediment composition can show great spatial and temporal heterogeneity, even  
10 on river reach scale, making it difficult to representatively sample and assess. Indeed, conventional sampling  
11 methods in such cases cannot describe well the variability of the bed surface texture due to the amount of energy  
12 and time they would require. In this manuscript, an attempt is made to overcome this issue introducing a novel  
13 image-based, Deep Learning algorithm and related field measurement methodology with potential for becoming  
14 a complementary technique for bed material samplings and significantly reducing the necessary resources. The  
15 algorithm was trained to recognise main sediment classes in videos that were taken underwater in a large river  
16 with mixed bed sediments, along cross-sections, using semantic segmentation. Videos were taken on 3 different  
17 sites in the Upper Section of the Hungarian Danube. One served for training the AI algorithm, while the other two  
18 were for validation. The introduced method is fast, i.e., the videos of 300-400-meter-long sections can be analysed  
19 within minutes, with very dense spatial sampling distribution. The goodness of the trained algorithm was evaluated  
20 mathematically and via intercomparison with other direct and indirect methods, focusing on the percentages of  
21 the detected sediment fractions. For the final evaluation, the sieving analysis of collected physical samples were  
22 considered as the ground truth. The results of the AI algorithm were promising, in 64% of the compared sampling  
23 points the difference were  $\leq 10\%$  from the sieved physical samples, while for the rest of the points it also did not  
24 exceed 20%. Besides, the spatial trend in the fraction changes was also well captured along the cross-sections,  
25 based upon the visual evaluation of the footages. Suggestions for performing proper field measurements are also  
26 given, furthermore, possibilities for combining the algorithm with other techniques are highlighted, briefly  
27 showcasing the multi-purpose of underwater videos for hydromorphological assessment.

28 **Keywords:** riverbed texture, underwater mapping, sediment classes, Artificial Intelligence, Deep Learning,  
29 image-based

### 30 **1 Introduction**

31 The physical composition of a riverbed plays a crucial role in fluvial hydromorphological processes, as a sort of  
32 boundary condition in the interaction mechanisms between the flow and the solid bed. Within these processes, the  
33 grains on the riverbed are responsible for multiple phenomena, such as flow resistance (Vanoni and Hwang, 1967;  
34 Zhou et al., 2021), stability of the riverbed (Staudt et al., 2018; Obodovskyi et al., 2020), development of bed  
35 armour (Rákóczi, 1987; Ferdowsi et al., 2017), sediment clogging (Rákóczi, 1997; Fetzer et al., 2017), fish shelter  
36 (Scheder et al., 2015), etc. Through these physical processes, the bed material composition has a determining  
37 effect on numerous river-uses, e.g., possibilities of inland waterway transport, drinking water supply through bank

38 filtration, the quality of riverine habitats, etc. Knowledge of riverbed morphology and sediment composition is  
39 therefore of major importance in river hydromorphology. In order to gain information about riverbed sediments,  
40 in situ field sampling methodologies are implemented.

41

42 Traditionally, bed material sampling methods are intrusive (i.e., sediment is physically extracted from the bed for  
43 follow-up analysis) and carried out via collecting the sediment grains one-by-one (areal, grid-by-number and  
44 pebble count methods, see e.g., Bunte and Abt, 2001; Guerit et al., 2018) or in a larger amount by a variety of  
45 grab samplers (volumetric methods, such as WMO, 1981; Singer, 2008). This is then followed by measuring their  
46 sizes individually on-site or transporting them to a laboratory for mass-sieving analysis (Fehr, 1987; Diplas, 1988;  
47 Bunte and Abt, 2001). These sampling procedures are time- and energy consuming, especially in large gravel and  
48 mixed bed rivers, where characteristic grain sizes can strongly vary both in time and space (Wolcott and Church,  
49 1991; USDA, 2007), requiring a dense sampling point allocation. The same goes for critical river reaches, where  
50 significant human impact led to severe changes in the morphological state of the rivers (e.g., the Upper section of  
51 the Hungarian Danube; Török and Baranya, 2017). When assessing bed material composition on a river reach  
52 scale, experts usually try to extrapolate from the samples, and describe larger regions of the bed (even several  
53 thousand m<sup>2</sup>) by data gathered in a few, several dozen points (see e.g., USDA, 2007; Haddadchi et al., 2018;  
54 Baranya et al., 2018; Sun et al., 2021). Gaining a representative amount of the sediment samples is also a critical  
55 issue. For instance, following statistical criteria such as those of Kellerhals and Bray (1971) or Adams (1979), a  
56 representative sample should weigh ten-to-hundred kg. Additionally, physical bed material sampling methods are  
57 unable to directly quantify important, hydromorphological features such as roughness or bedforms (Graham et al.,  
58 2005). Due to these constraints, surrogate approaches have recently been intensively tested to analyse the riverbed  
59 (see Chapter 2). Unlike the conventional methods, these techniques are non-intrusive and rely on computers and  
60 other instrumentation to decrease the need of human intervention and speed up the analyses.

61

62 One group of the surrogate approaches is the acoustic methods, where an acoustic wave source (e.g., an Acoustic  
63 Doppler Current Profiler; ADCP) is pointed towards the riverbed from a moving vessel, emitting a signal. The  
64 strength and frequency of this signal is measured while it passes through the water column, reflecting back to the  
65 receiver from the sediment transported by the river, and finally from the riverbed itself. This approach is fast and  
66 larger areas can be covered relatively quickly (Grams et al., 2013). While it has already become widely used for  
67 describing sediment movement (i.e., suspended sediment, Guerrero et al., 2016; bedload, Muste et al., 2016; and  
68 indirectly flow velocity; Shields and Rigby, 2005) and channel shape (Zhang et al., 2008), it has not reached  
69 similar breakthrough for riverbed material analysis. Researchers found that it is necessary to apply instrument  
70 specific coefficients to convert the signal strength, and these coefficients can only be derived by first validating  
71 each instrument using collected sediment samples with corresponding ADCP data. Moreover, the method is  
72 sensitive to the bulk density of the sediment and to bedforms (Shields, 2010), while it is also not possible to  
73 measure individual grains this way (Buscombe et al., 2014a; 2014b). Hence, the separation of surface roughness  
74 from the effects of bedforms is also not possible. Clay and silt patches could be separated with the acoustic  
75 approach, but gravel could not be distinguished strongly from sand.

76

77 Another group of the surrogate approaches is the application of photography (Adams, 1979; Ibbekken and  
78 Schleyer, 1986) and later computer vision or image-processing techniques. During the last two decades, two major  
79 subgroups emerged: one uses object- and edge detection (by finding abrupt changes in intensity and brightness of  
80 the picture, segmenting objects from each other; Sime and Ferguson, 2003; Detert and Weitbrecht, 2013), and the  
81 other one analyses the textural properties of the whole image, using autocorrelation and semi-variance methods  
82 to define empirical relationship between image texture and the grain sizes of the photographed sediments (Rubin,  
83 2004; Verdú et al., 2005). The above-mentioned image processing approaches were very time consuming and  
84 required mostly site-specific manual settings, however, a few transferable and more automated techniques have  
85 also been developed recently (e.g., Graham et al., 2005; Buscombe, 2013). Even though there is a continuous  
86 improvement in the applied image-based bed sediment analysis methods, there are still major limitations the users  
87 face with, such as:

88

- 89 • Most of the studies (all the ones listed above) focuses on gravel bed rivers, and only a few exceptions  
90 can be found in the literature where sand is also accounted for (texture-based methods; e.g.:  
91 Buscombe, 2013).
- 92 • The adaptation environment was typically non-submerged sediment, instead of underwater  
93 conditions (a few exceptions: Chezar and Rubin, 2004; Warrick et al., 2009).
- 94 • The computational demand of the image processing is high (e.g., one to ten minutes per image;  
95 Detert and Weitbrecht, 2013).
- 96 • The analysis requires operator expertise (higher than in case of any conventional method).
- 97 • There is an inherent pixel- and image resolution limit (Buscombe and Masselink, 2008; Cheng, 2015;  
98 Purinton and Bookhagen, 2019). The finer the sediment, the higher resolution of the images should  
99 be (higher calculation time), or they must be taken from a closer position (smaller area and sample  
100 per image).

101

102 Nowadays, with the rising popularity of Artificial Intelligence (AI), several Machine Learning (ML) techniques  
103 have been implemented in image recognition as well. The main approaches of segmentation contra textural  
104 analysis still remain; however, an AI defines the empirical relationship between the object sizes (Igathinatane et  
105 al., 2009; Kim et al., 2020) or texture types (Buscombe and Ritchie, 2018) in the images and their real sizes. In  
106 the field of river sedimentology a few examples can already be found, where ML (e.g., Deep Learning; DL) was  
107 implemented. For instance, Rozniak et al. (2019) developed an algorithm for gravel-bed rivers, performing  
108 textural analysis. With this approach, information is not gained on individual grains (e.g., their individual shape  
109 and position), but rather the general grain size distribution (GSD) of the whole images. At certain points of the  
110 studied river basins, conventional physical samplings (pebble count) were performed to provide real GSD  
111 information. Using this data, the algorithm was trained (with ~1000 images) to estimate GSD for the rest of the  
112 study site, based on the images. The method worked for areas where grain diameters were larger than 5 mm, and  
113 the sediment was well-sorted. The developed method showed sensitivity to sand coverage, blurs, reduced  
114 illuminations (e.g., shadows) and white pixels. Soloy et al. (2020) presented an algorithm which used object  
115 detection on gravel- and cobble covered beaches to calculate individual grain sizes and shapes. 46 images were  
116 used for the model training, however, the number of images were multiplied with data augmentation (rotating,

117 cropping, blurring the images; see Perez and Wang, 2017) to enhance the learning session and increase the input  
118 data. The method was able to reach a limited execution speed of a few seconds per m<sup>2</sup> and adequately measured  
119 the sizes of gravels. Ren et al. (2020) applied an ensemble bagging-based Machine Learning (ML) algorithm to  
120 estimate GSD along the 70 km long Hanford Reach of the Columbia River. Due to its economic importance, a  
121 large amount of measurement data has been accumulated for this study site over the years, making it ideal for  
122 using ML. By the time of the study, 13,372 scaled images (i.e., their millimetre/pixel ratio was known) were taken  
123 both underwater and in the dry zones, covering approx. 1 m<sup>2</sup> area each. The distance between the image-sampling  
124 points was generally between 50-70 m. An expert defined the GSD (8 sediment classes) of each image by using a  
125 special, visual evaluation-classification methodology (DeLong and Brusven, 1991; Geist et al., 2000). This dataset  
126 was fed to a ML algorithm along with their corresponding bathymetric attributes and hydrodynamic properties,  
127 simulated with a 2D hydrodynamic model. Then, it was tested to predict the sediment classes based on the  
128 hydrodynamic parameters only. The algorithm performed with a mean accuracy of 53%. Even though this method  
129 was not image-based (only indirectly, via the origin of the GSD data), it highlighted the possibilities of an AI for  
130 a predictive model, using a high-dimensional dataset. Having such a large data of grain size information can be  
131 considered exceptional and takes a huge amount of time to gather, even with the visual classification approach  
132 they adapted. Moreover, this was still considered spatially sparse information (point-like measurements, 1 m<sup>2</sup>  
133 covered area/image dozens of meters away from each other). Buscombe (2020) used a set of 400 scaled images  
134 to train a AI algorithm on image texture properties, using another image-processing method (Barnard et al., 2007)  
135 for validation. The algorithm reached a good result for not only gravel, but sand GSD calculation as well,  
136 outperforming an earlier, but promising, texture-based method (wavelet analysis; Buscombe, 2013). In addition,  
137 the method required fewer calibration parameters than the wavelet image-processing approach. The study also  
138 foresaw the possibility to train an AI which estimates the real sizes of the grains, without knowing the scale of  
139 one pixel (mm/pixel ratio) if the training is done properly. The AI might learn unknown relationships between the  
140 texture and sizes if it is provided with a wide variety (images of several sediment classes) and scale (mm/pixel  
141 ratio)) of dataset (however, it is also prone to learn unwanted biases). Recently, Takechi et al. (2021) further  
142 elaborated on the importance of shadow- detection and removal, using a dataset of 500 pictures for training a  
143 texture-based AI, with the help of an object-detecting image-processing technique (Basegrain; Detert and  
144 Weitbrecht, 2013). The previously presented studies, applying ML and DL techniques, significantly contributed  
145 to the development and improvement of surrogate sampling methods, incorporating the great potential in AI.  
146 However, there are still several shortcomings to these procedures. Firstly, none of the image-based AI studies  
147 used underwater recordings, even though the underwater environment offers completely different challenges.  
148 Secondly, the training images were always scaled, i.e., the sizes of the grains could be easily reconstructed, which  
149 is again complicated to accomplish in a river. Lastly, they were not adapted for continuous (i.e., spatially dense)  
150 measurement, but rather focused on a sparse grid-like approach.

151  
152 The goal of this manuscript is to further investigate the applicability of image processing as a surrogate method,  
153 and attempt to break through the above mentioned shortcomings of the AI-based approaches. Hence, we introduce  
154 a riverbed material analysing, Deep Learning technique and field measurement methodology, along with our first  
155 set of results. The introduced technique aims to eventually become a tool for exploratory mapping of the riverbed,  
156 by detecting sedimentation features (e.g., deposition zones of fine sediment, bed armour) and helping decision

157 making for river sedimentation management. Also, the long-term hypothesis of the authors includes the creation  
158 of an image-based measurement methodology, where underwater videos of the riverbed could serve multiple  
159 sediment related purposes simultaneously. Part of which is the current approach for mapping the riverbed material  
160 texture and composition. Others include measuring the surface roughness of the bed (Ermilov et al., 2020) and  
161 detecting bedload movement (Ermilov et al., 2022).

162

163 Compared to the earlier studies introduced earlier, the main novelty of our manuscript is that both the training and  
164 analysed videos are recorded underwater, continuously along cross-sections of a large river. Furthermore, the  
165 training is unscaled, i.e., the camera-riverbed distance could vary while recording the videos, without considering  
166 image-scale. Moreover, compared to the relatively low number of training images in most of the above referred  
167 studies, we used a very large dataset (~15000) of sediment images for the texture-based AI, containing mostly  
168 sand, gravel, cobble, and to a smaller extent: bedrock together with some other, non-sediment related objects.

169

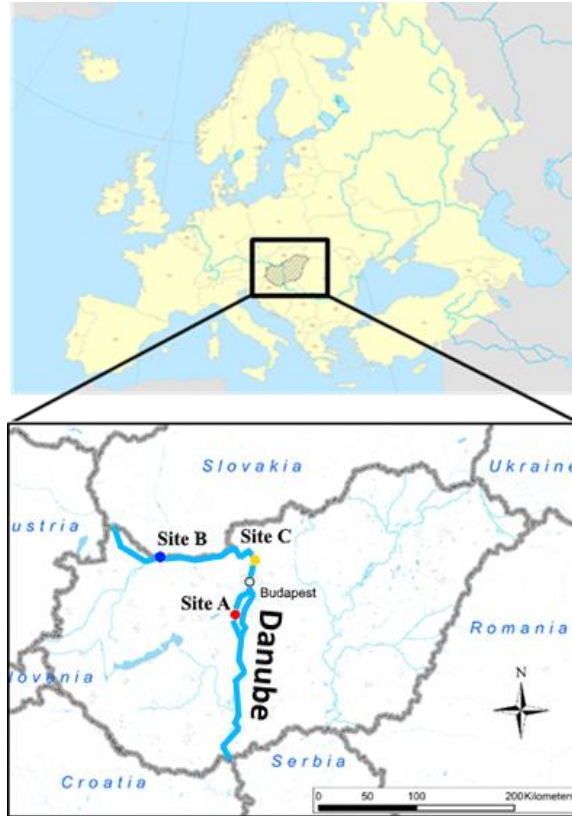
170 In this current manuscript, first, a literature review is given to better understand the current state of surrogate  
171 bedmaterial sampling approaches and their research, gradually leading up to the method of this manuscript and  
172 highlighting its relevance. In the third chapter the case studies and the methodology are introduced in detail. The  
173 third chapter presents the results and their evaluation, followed by a discussion about the challenges, the novelty  
174 and possible continuations of the method. A brief discussion is also given on how the method can support  
175 traditional methods and what kind of additional hydromorphological parameters can be provided by such videos,  
176 uniquely improving the toolkits of sedimentation engineering. Finally, the main conclusions of the manuscript  
177 are drawn.

178

## 179 **3 Methods**

### 180 **3.1 Case studies**

181 The results presented in this study are based on riverbed videos taken during three measurement campaigns, in  
182 sections of the Danube River, Hungary. The first one was at Site A, Ercsi settlement (~ 1606 rkm), the second one  
183 was at Site B, Gönyű settlement (~ 1791 rkm), and the third was at Site C, near to Göd settlement (~ 1667 rkm)  
184 (Fig. 1).



185  
186  
187

Figure 1: The location of the riverbed videos, where the underwater recordings took place. All sites were located in Hungary, Central Europe. The surveys were carried out on the Danube River, Hungary's largest river.

188  
189  
190  
191  
192  
193  
194

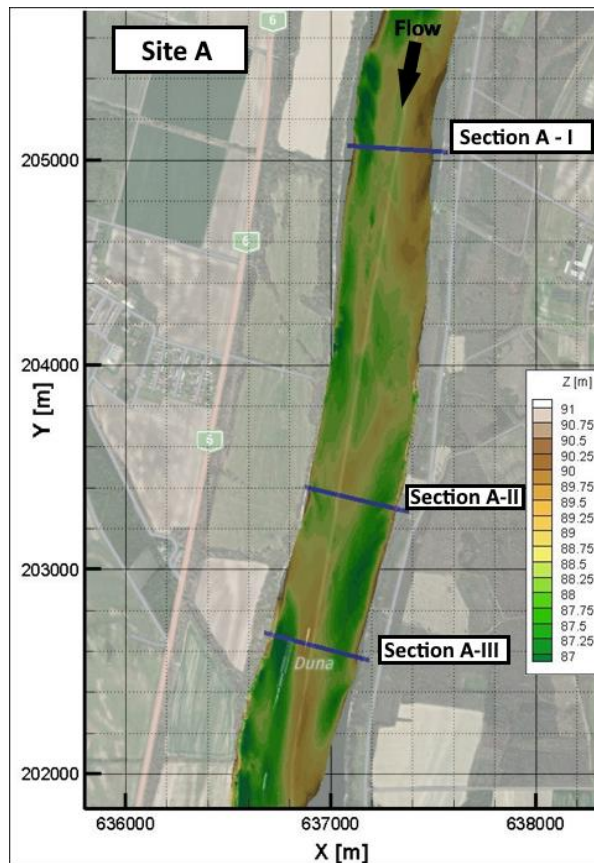
The training of the AI was done using the video images of Site C and a portion of A (test set; see later in Chapter 3.3), while Site B and the rest of the images from A served for validation. The measurements were carried out during daytime, at mid-water regime ( $Q = 1900 \text{ m}^3/\text{s}$ ) in case of Site A, and low water regime ( $Q = 1350 \text{ m}^3/\text{s}$ ) at Site B, similarly to Site C ( $Q = 700 \text{ m}^3/\text{s}$ ). This latter site served only for increasing the training image dataset (i.e., conventional samplings were not carried out at the time of recording the videos), thus we do not go into further details with it for the rest of the manuscript, but the main characteristics are listed in Table 1.

	Site A	Site B	Site C
$Q_{\text{survey}} [\text{m}^3/\text{s}]$	1900	1350	700
$B_{\text{survey}} [\text{m}]$	300 – 450		
$H_{\text{mean, survey}} [\text{m}]$	3.5 - 4.5		
$S_{\text{survey}} [\text{cm}/\text{km}]$	15		
$SSC_{\text{survey}} [\text{mg}/\text{l}]$	25	20	14
<b>Characteristic sediment riverbed</b>	gravel, sandy gravel	gravel, gravelly sand	gravel, sandy gravel
$Q_{\text{annual, mean}} [\text{m}^3/\text{s}]$	2000	2200	1400
$Q_{1\%} [\text{m}^3/\text{s}]$	5300	5500	4700

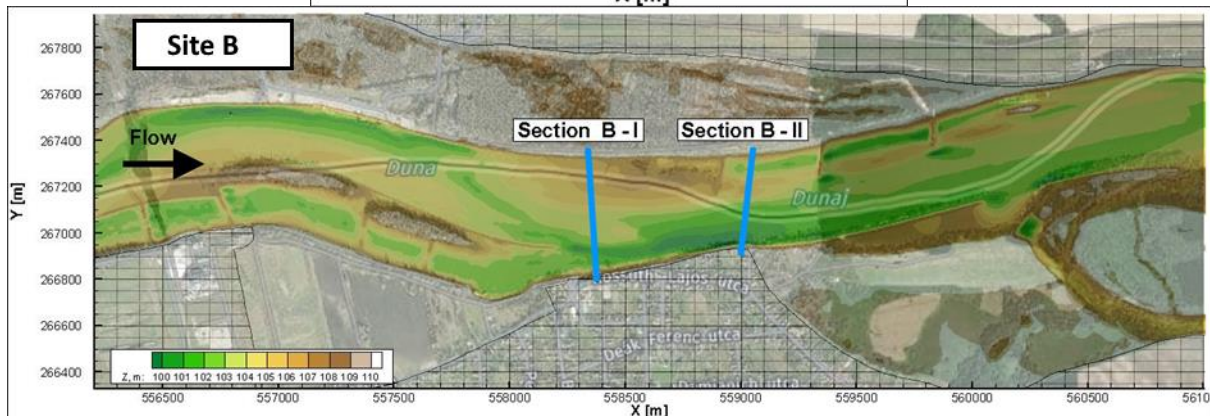
195  
196  
197  
198

Table 1: Main hydromorphological parameters of the measurement sites.  $Q_{\text{survey}}$ : discharge during survey;  $B_{\text{survey}}$ : river width during survey;  $H_{\text{mean, survey}}$ : mean water depth during the survey;  $S_{\text{survey}}$ : riverbed slope during survey;  $SSC_{\text{survey}}$ : mean suspended sediment concentration during the survey;  $Q_{\text{annual, mean}}$ : annual-mean of the discharge at the site;  $Q_{1\%}$ : discharge of 1% probability.

199 As underwater visibility conditions are influenced by the suspended sediment, the characteristics of this sediment  
 200 transport is also included in Table 1 ( $SSC_{survey} - \text{susp. sed. concentration}$ ). The highest water depths were around  
 201 6-7 m in all cases. In Site A, measurements included mapping of the riverbed with a camera along three separate  
 202 transects (Fig. 2). At Site B, two transects were recorded.



203



204

205

206

207

**Figure 2: Bathymetry of Site A and B. The measurement cross-sections are also marked. The vessel moved along these lines from one bank to the other, while carrying out ADCP measurement and recording riverbed videos. Physical bed material samples were also collected in certain points of these sections.**

208

### 209 3.2 Field data collection

210

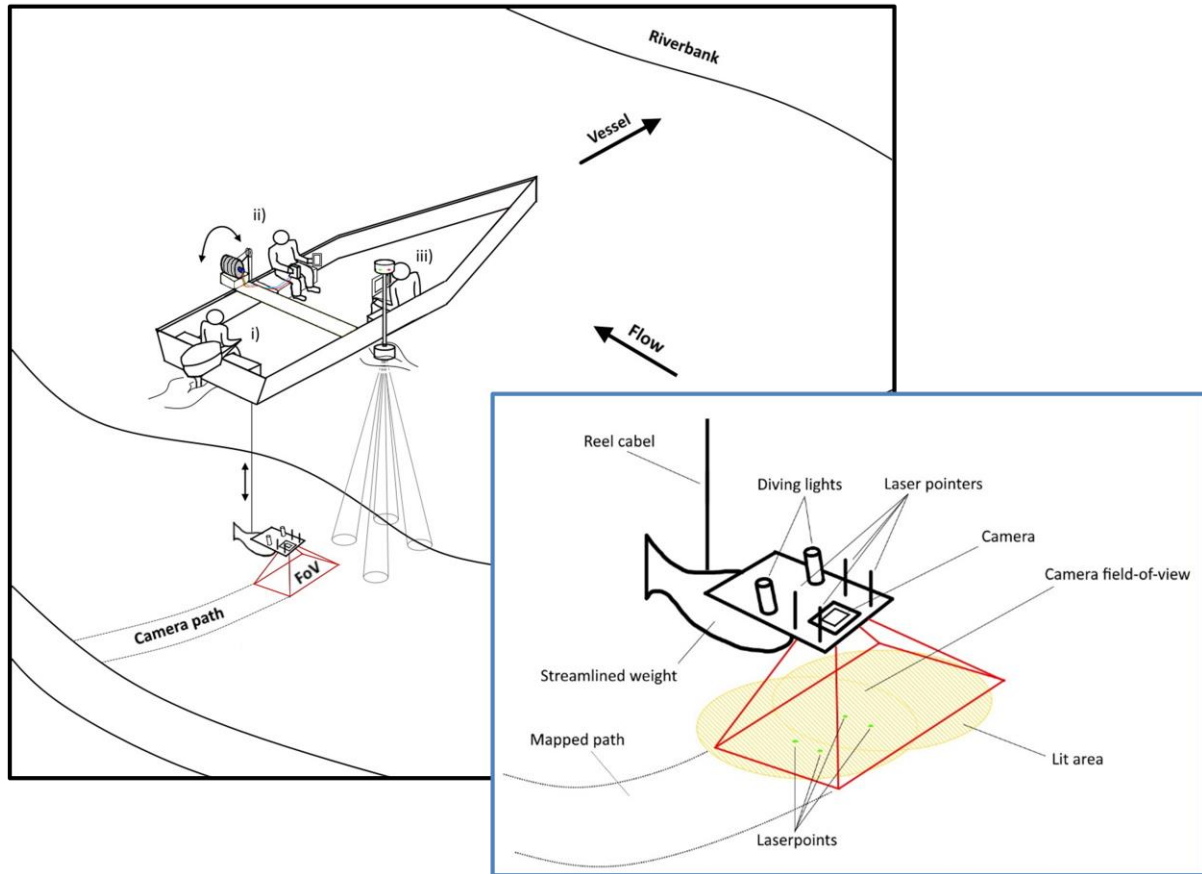
211

212

Fig. 3 presents a sketch of the measurement process with the equipment and a close-up of the underwater instrumentation. During the field measurements, the camera was attached to a streamlined weight (originally used as an isokinetic suspended sediment sampler) and lowered into the water from the vessel by an electric reel. The

213 camera was positioned perpendicularly to the water and the riverbed, in front of the nose of the weight. Next to  
214 the camera, two diving lights worked as underwater light sources, focusing into the camera's field of view (FoV).  
215 In addition, four laser pointers were also equipped in hand-made isolation cases to provide possible scales for  
216 secondary measurements. They were also perpendicular to the bottom, projecting their points onto the underwater  
217 camera field of view. Their purpose was to ensure a visible scale (mm/pixel ratio) in the video footages for  
218 validation. During the measurement procedure, a vessel crossed the river slowly through river transects, while the  
219 position of the above detailed equipment was constantly adjusted by the reel. Simultaneously, ADCP and RTK  
220 GPS measurement were carried out by the same vessel, providing water depth, riverbed geometry, flow velocity,  
221 ship velocity and position data. Based on this information and by constantly checking the camera's live footage  
222 on deck, the camera was lowered or lifted to keep the bed in camera sight and avoid colliding with it. The sufficient  
223 camera – riverbed distance depended on the suspended sediment concentration near the bed and the used  
224 illumination. The reel was equipped with a register, with its zero adjusted to the water surface. This register was  
225 showing the length of cable already released under the water, effectively the rough distance between the water  
226 surface and the camera (i.e., the end of the cable). Of course, due to the drag force this distance was not vertical,  
227 but this value could be continuously compared to the water depth measured by the ADCP. Differencing these two  
228 values, an approximation for the camera – riverbed distance was given all time. The sufficient difference could  
229 be established by monitoring the camera footage while lowering the device towards the bed. This value was then  
230 to be maintained with smaller corrections during the survey of the given cross-section, always supported by  
231 observing the camera recording, and adjusting to environmental changes. The vessel's speed was also adjusted  
232 based on the video and slowed down if the video was blurry or the camera got too far away from the bed (see later  
233 in Chapter 4.3). The measurements required three personnel to i) drive the vessel, ii) handle the reel, adjust the  
234 equipment position, and monitor the camera footage, iii) monitor the ADCP data, while communicating with the  
235 other personnel (see Fig. 3).





236  
237  
238  
239

**Figure 3: Left: sketch of the measurement process. The vessel was moving perpendicular to the riverbank along a cross-section (i). A reel was used to lower a camera close to the riverbed (ii). Simultaneously, the bed topography and water depth were measured by an ADCP (iii). Right: Close-up sketch of the underwater instrumentation.**

240  
241  
242  
243  
244  
245  
246  
247  
248  
249  
250  
251  
252

The video recordings were made with a GOPRO Hero 7 and a Hero 4 commercial action cameras. Image resolutions were set to 2704x2028 (2.7K) with 60 frame per second (fps) and 1920x1080 (1080p) with 48 fps, respectively. Other parameters were left at their default (see GOPRO 2014; 2018), resulting in slightly different quality of produced images between the two cameras. We found that a 0.2-0.45 m/s vessel speed with 60 fps recording frequency was ideal to retrieve satisfactory images in a range of 0.4-1.6 m camera-bed distances. This meant approximately 15 minutes long measurements per transects. Further attention needed to be paid to the reel and its cable during the crossing when the equipment was on the upstream side of the boat. If the flow velocities are relatively high (compared to the total submerged weight of the underwater equipment), the cable can be pressed against the vessel-body due to the force from the flow itself, causing the reel cable to jump to the side and leave its guide. This results in the equipment falling to the riverbed and the measurement must be stopped to reinstall the cable. For illumination, a diving light with 1500 lumen brightness and 75° beam divergence, and one with 1800 lumen and 8° were used. The four lasers for scaling had 450-520 nm (purple and green) wavelength and 1-5 mW nominal power. Power supply was ensured with batteries for all instruments.

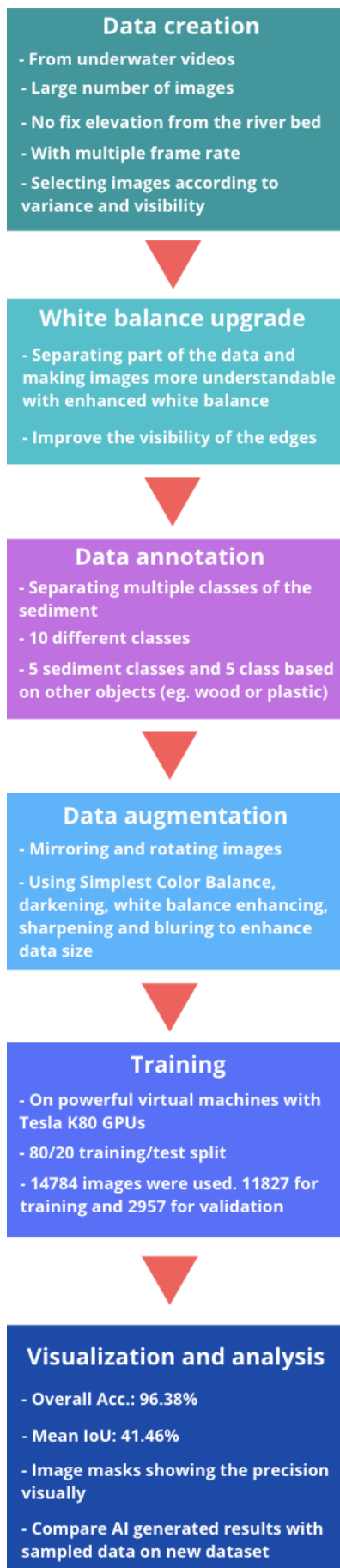
253  
254  
255  
256  
257  
258

At Site A and Site B, conventional bed material (physical) samplings were also carried out by a grabbing (bucket) sampler along the analysed transects. At each cross-section 4-5 samples were taken, with one exception where we had 10. The measured GSDs were used to validate results of the AI algorithm. Separately, a visual evaluation of the videos was also carried out, where a person divided the transects into subsections based on their dominant sediment classes, after watching the footages.

### 259 3.3 Image analysis: Artificial Intelligence and the wavelet method

260 In this study, we built on the former experiences of the authors, using Benkó et al., 2020 as a proof-of-concept,  
261 where the developed algorithm was applied for analysing drone videos of a dry riverbed. The same architecture  
262 was used in this manuscript, which is based on the widely used Google's DeeplabV3+ Mobilnet, in which many  
263 novel and state-of-the-art solutions are implemented (e.g., Atrous Spatial Pyramid Pooling; Chen et al., 2018).  
264 The model was implemented with Pytorch, exploiting its handy API and backward compatibility. The main goal  
265 was to build a deep neural network model which can recognise and categorise (via semantic segmentation; Chen  
266 et al., 2018) at least three main sediment size classes, i.e., sand, gravel and cobble, in the images, while being  
267 quickly deployable. The benefit of the introduced method compared to conventional imagery methods lies in the  
268 potential of automation and increased speed. If the annotation and training is carried out thoroughly, analysing  
269 further videos can run effortlessly, while the computation time can be scaled down either vertically (using stronger  
270 GPUs) or horizontally (increasing the number of GPUs; if parallel analysis of images is desired). In this study a  
271 TESLA K80 24GB GDDR5 348bit GPU, an Intel Skylake Intel® Xeon® Gold 6144 Processor (24.75M Cache,  
272 3.50 GHz) CPU with 13GB RAM was used. Also, contrary to other novel image-processing approaches in riverine  
273 sediment research (Buscombe, 2013; Detert and Weitbrecht, 2013), the deep convolutional neural network is  
274 much less limited by image resolution and mm/pixel ratios, because it does not rely on precise pixel count. This  
275 is an important advantage to be exploited here, as we perform non-scaled training and measurements with the AI,  
276 i.e., camera-bed distance constantly changed, and size-reference was not used in the images by the AI.

277  
278 Fig. 4 presents the flowchart of our AI-based image processing methodology. The first step after capturing the  
279 videos was to cut them into frames, during which the videos were exploded into sequential images. Brightening  
280 and sharpening filters were applied on the images to improve their quality. Next, the ones with clearest outlines  
281 and best visibility were chosen. This selection process was necessary because this way the delineation process  
282 (learning the prominent characteristics of each class) can be executed accurately, without the presence of  
283 misleading or confusing images, e.g., blurry or dark pictures where the features are hard to recognise. For training  
284 purposes, we chose three footages from different sections each being ~15 minutes long with 60 fps and 48 fps,  
285 resulting in 129 600 frames. In fact, no such large dataset was needed due to the strong similarity of the consecutive



frames. The number of images to be annotated and augmented were therefore decreased to ~2000. We also performed a white balance correction on some of the images to improve visibility, making it even easier to later define the sediment class boundaries. We used an additional algorithm to generate more data, with the so-called Simplest Colour Balance method (Limare et al., 2011). It is a simple, but powerful histogram equalisation algorithm which helps to equalise the roughness in pixel distribution.

These steps were followed by the annotation, where we distinguished ten classes. Annotation was carried out by a trained personnel, not by the authors, and performed with the help of an open-source software called PixelAnnotationTool (Breheret, 2017), which enables the user to colour mask large parts of an image based on colour change derivatives (i.e., colour masking part of the images which belong to the same class, e.g., purple/red – sand, green – gravel, yellow – cobble, etc.). The masks and outlines were drawn manually, together with the so-called watershed annotation. That is, when a line was drawn, the algorithm checked for similar pixels in the vicinity and automatically annotated them with the same class. The annotation was followed by a data augmentation step where beside mirroring, cropping, rotating the images (to decrease the chance of overfitting), we also convolved them with different filters. These filters added normally distributed noise to the photos to influence the watershed algorithm and applied sharpening, blurring, darkening, and white balance enhancement. Thus, at the data level, we tried to ensure that any changes in water purity, light, and transparency, as well as colour changes, were adequately represented during training. Images were uniformly converted to 960x540 resolution, scaling them down to make them more usable to fit in the GPU’s memory. The next step was to convert all the images from RGB (Red-Green-Blue) based colour to grayscale. This is important because colour images have 3-channels, so that they contain a red, a green, and a blue layer, while grayscale images’ pixel can only take one value between 0 and 255. With this colour conversion we obtained a threefold increase in computational speed. In total, a dataset of 14,784 images was prepared (from the ~2000 images of the 4 training videos). The next step was to separate this into training and validation sets. In this study, 80% of the data was used for training the Artificial Intelligence, while 20% was to validate the training. It was important to mix the images so that the algorithm selects batches in a pseudorandom manner during training, thus preventing the model from being overfitted.

Figure 4: Flowchart of the applied methodology.

326 Finally, after several changes in the hyperparameters (i.e., tuning), the evaluation and visualisation of the training  
327 results were performed. Tuning is a general task to do when building Deep Learning Networks, as these  
328 hyperparameters determine the structure of the network and the training process itself. Learning rate, for example,  
329 describes how fast the network refreshes, updates itself during the training. If this parameter is set too high, the  
330 training process finishes quickly, but convergence may not be reached. If it is too low, the process is going to be  
331 slow, but it converges. For this reason, nowadays the learning rate decay technique is used, where one starts out  
332 with a large learning rate, then slowly reduces it. The technique generally improves optimization and  
333 generalization of the Deep Learning Networks (You et al., 2019). In our case, learning rate was initialised to 0.01,  
334 with 30000 iteration steps, and the learning rate was reset after every 5000 iterations with a decay of 0.1. Another  
335 important parameter was the batch size, which sets the number of samples fed to the network before it updates  
336 itself. Theoretical and empirical evidence suggest that learning rate and batch size are highly important for the  
337 generalization ability of a network (He et al., 2019). In our study, a batch size of 16 was used (other general values  
338 in the literature are 32, 64, 128, 256). We used a cross-entropy loss function.

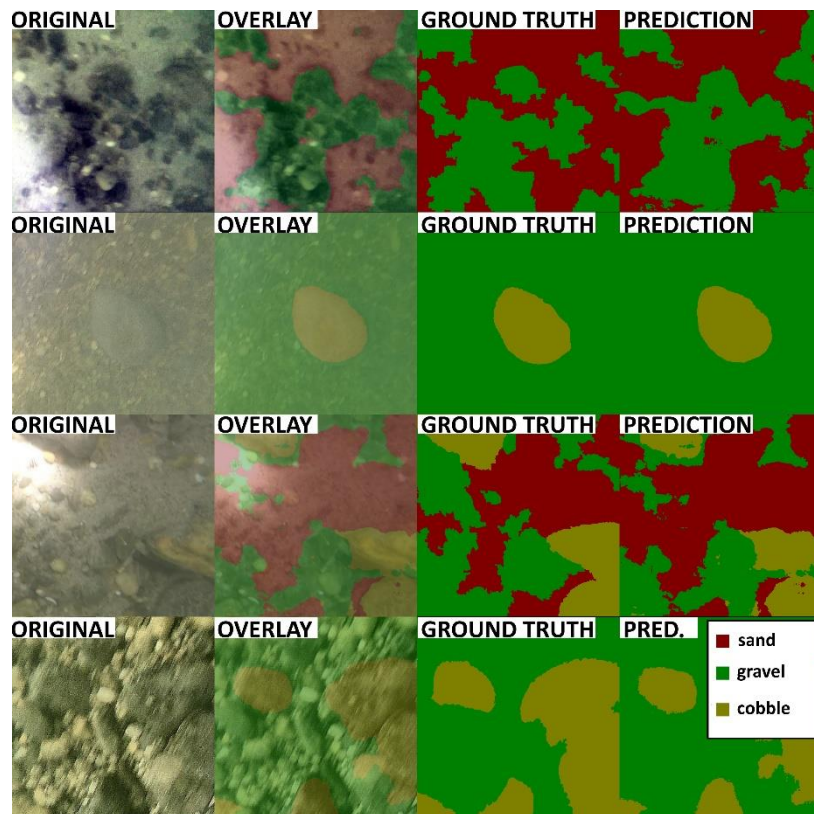
339  
340 As previously mentioned, the training of the AI was managed without scaling, without the need for equipped  
341 lasers. However, we intended to use the laser pointers to provide a spatial scale for the recorded videos, as a  
342 secondary validation. As the lasers were not functioning as we originally hoped, we could not use them constantly  
343 during the cross-sectional surveys and could not aim for transactional scaling and validation this way. Instead, we  
344 diverted to validation in the points of the physical samplings as we could use the lasers in a few, selected points  
345 only. We used a textural image-processing method to analyse the video images of these sampling spots. For this,  
346 the already mentioned, transferable wavelet-based signal- and image-processing method was chosen. The method  
347 enables to calculate the image-based grain size distribution of the selected pictures. The grey-scale intensity is  
348 analysed through pixel-rows and -columns of the image and handled as individual signals. Then, instead of  
349 Fourier-transform, the less-constrained wavelet-transform is applied to decompose them. Finally, calculating the  
350 power spectra and the sizes (from pixel to millimetre, using the scale) of the wavelet components (each wavelet  
351 describes an individual grain) produces the grain size distribution for the given image. Beforehand, this method  
352 was proved to be the most efficient, non-AI image-processing method for mixed sediments (Buscombe, 2013;  
353 2020) and was already tested for underwater circumstances in an earlier study by the authors of present manuscript  
354 (Ermilov et al., 2020).

## 355 **4 Results and discussion**

### 356 **4.1 Evaluation of the training**

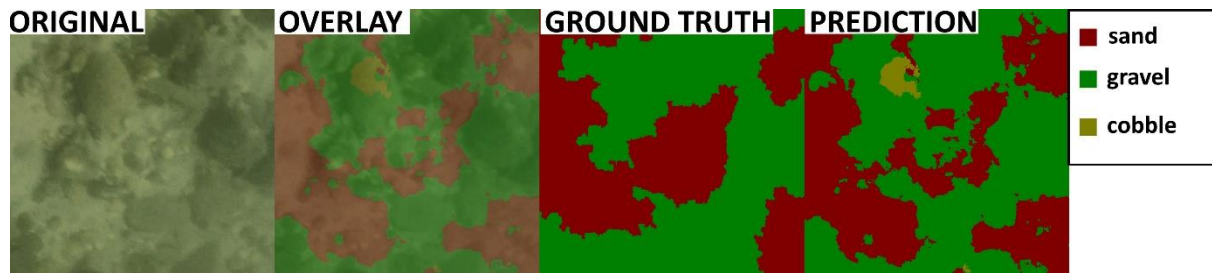
357 To evaluate the training process, the image series used for the training was analysed by the developed Deep  
358 Learning algorithm. Fig. 5 shows results of original images (from the validation set), their ground truth (annotation  
359 by the training personnel), as well as the AI prediction (result of the model). The overlays of the original and the  
360 predicted images are also shown for better visualization. Calculating the over-all pixel accuracy (i.e., the percent  
361 of pixels that were correctly classified) returned a satisfactory result with an average 96% match. As this parameter  
362 in object detection and Deep Learning is not a stand-alone parameter (i.e., it can still be high even if the model  
363 performs poorly), the mean IoU (intersection-over-union or Jaccard index) was also assessed, indicating the

364 overlap of ground truth area and prediction area, divided by their union (Rahman and Wang, 2016). This parameter  
 365 showed a much slighter agreement of 41.46%. Interestingly, there were cases, where the model gave better result  
 366 than the annotating personnel. While this highlighted the importance of thorough and precise annotation work, it  
 367 also showcased that the number of poor annotations was relatively low, so that the algorithm could still carry out  
 368 correct learning process and later detections, while not being severely affected by the mistake of the training  
 369 personnel. Fig. 6 showcases an example for this: the correct appearance of cobble (yellow) in the prediction, even  
 370 though the user (ground truth) did not define it during the training. As a matter of fact, these positive errors also  
 371 decrease the IoU evaluation parameter, even though they increase the performance of the AI on the long term.  
 372 Hence, this shows that pure mathematical evaluation may not describe the model performance entirely.  
 373 Considering that others also reported similar experience with Deep Learning (Lu et al., 2018) and the fact that  
 374 40% and 50% are generally accepted IoU threshold values (Yang et al., 2018; Cheng et al., 2018; Padilla et al.,  
 375 2020), we considered the 41.46% acceptable. The general quality of our underwater images may have also played  
 376 a role in lowering the IoU result.



377  
 378 Figure 5: Example comparisons of ground truth (taught pattern, 3<sup>rd</sup> column) and AI predicted (learnt pattern, 4<sup>th</sup>  
 379 column) sediment classes from the training videos showing satisfactory results. The 1<sup>st</sup> column shows raw images, while  
 380 the 2<sup>nd</sup> column overlays the result of the AI detection on the raw image for better visual context.

381  
 382  
 383



384  
 385 **Figure 6: Example comparison of ground truth (taught) and AI predicted (learnt) sediment classes from the training,**  
 386 **in case of training personnel mistake during the annotation.**

387 **4.2 Intercomparison of methods**

388 In each masked image, the occurring percentage of the given class (i.e., the percentage of the pixels belonging to  
 389 that class/colour mask, compared to the total number of pixels in the image) was calculated and used as the fraction  
 390 percentage in that given sampling point. These sediment classes reconstructed by the AI were then compared to  
 391 three alternative results: i) visual estimation, ii) GSD resulted from conventional grab sampling, iii) wavelet-based  
 392 image-processing. In the followings, results from two cross-sections will be shown, one from Site A, the video  
 393 used for the training, and one from Site B, being new for the AI. An averaging window of 15 m was applied on  
 394 each cross-sectional AI result to smoothen and despiked the dataset.

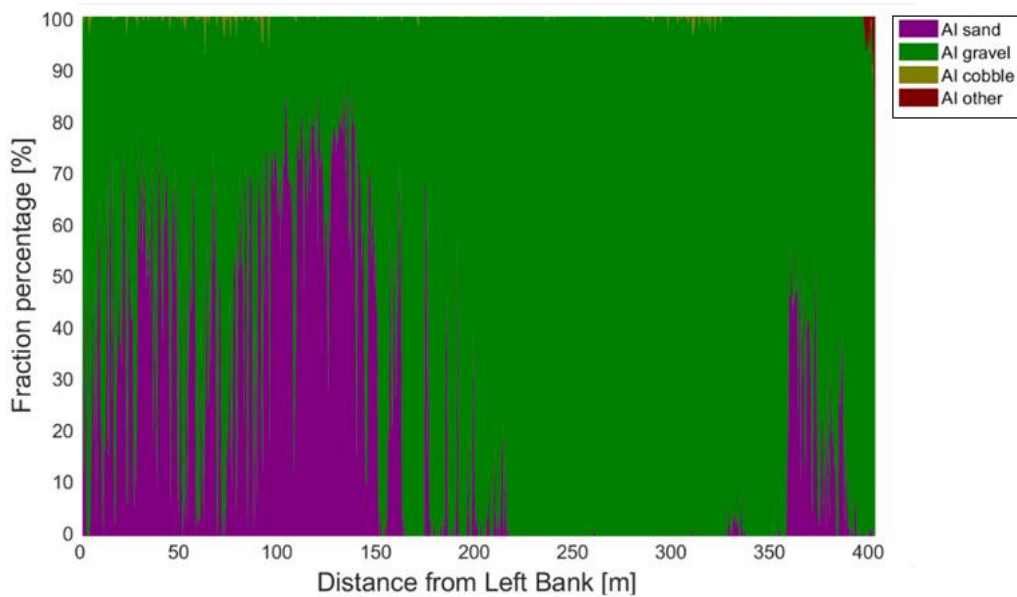
395  
 396 In Fig. 7, the path of the vessel can be seen in Section A - II, at Site A. The path was coloured based on the visual  
 397 evaluation of the riverbed images. The different colours represent the dominant sediment type seen at the given  
 398 point of the bed. The locations of the physical bed material samplings are also shown (see yellow markers). Fig.  
 399 8 presents the raw (i.e., before moving-average) results of the AI detection of each analysed image along Section  
 400 A - II. Currently, our approach is sensitive and large spikes, differences can occur in the AI detection between  
 401 consecutive, slightly displaced video frames. Due to this, and the fact that there is uncertainty in the coordinates  
 402 of the underwater photos and their corresponding physical samples, it is not recommended to carry out  
 403 comparisons by selecting certain image and its AI detection. Instead, we applied a moving average-based  
 404 smoothing for each raw, cross-sectional AI detection, with a window-size corresponding to 15 m. These moving-  
 405 averages are the ones being compared later in the sampling points to the physical sampling and the wavelet  
 406 method. For illustration purposes, we provided the raw AI detections of all the sampling point images, even though  
 407 their result may not be representative of their corresponding moving-average values. Fig. 9 shows the cross-  
 408 sectional visual classification compared to the AI-detected sediment fractions in percentage after applying  
 409 moving-average (i.e., the smoothed version of Fig. 8). The noises are mostly caused by sudden changes in lighting  
 410 conditions. It happens either from losing visual on the riverbed momentarily due to sudden topography changes  
 411 or from increased suspended sediment concentration.





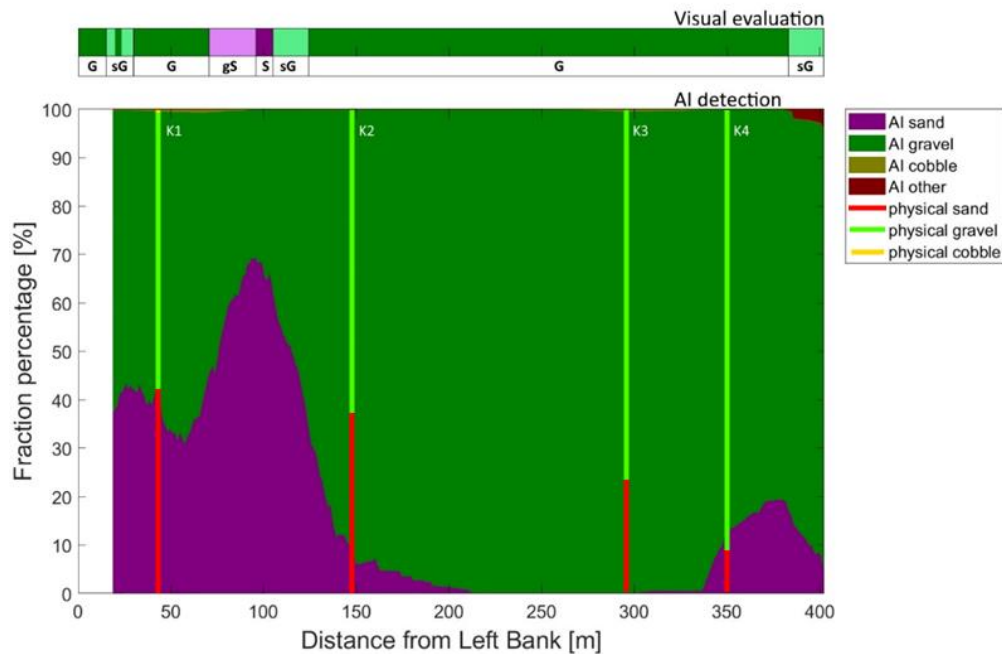
412  
 413 **Figure 7: The path of the vessel and camera in Section A - II, Site A. The polyline is coloured based on the sediment**  
 414 **features seen during visual evaluation of the video. Yellow markers are the locations of physical bed material samplings.**  
 415 **(Map created with Google Earth Pro)**

416



417  
 418 **Figure 8: The sediment fraction percentage results of every image, analysed by the AI along Section A - II. While the**  
 419 **trends are apparent, the sensitivity of the method at its current state can be observed. AI result before applying moving-**  
 420 **averaging.**

421



423  
 424 **Figure 9: Section A - II. The visual evaluation of the dominant sediment features in the video (top) compared to**  
 425 **sediment fraction percentage, recognised by the AI (bottom). AI result after applying moving-averaging. The visual**  
 426 **evaluation included four classes: gravel – G, sandy gravel – sG, gravelly sand – gS, sand – S.). The fractions of the**  
 427 **physical samples are shown as verticals.**

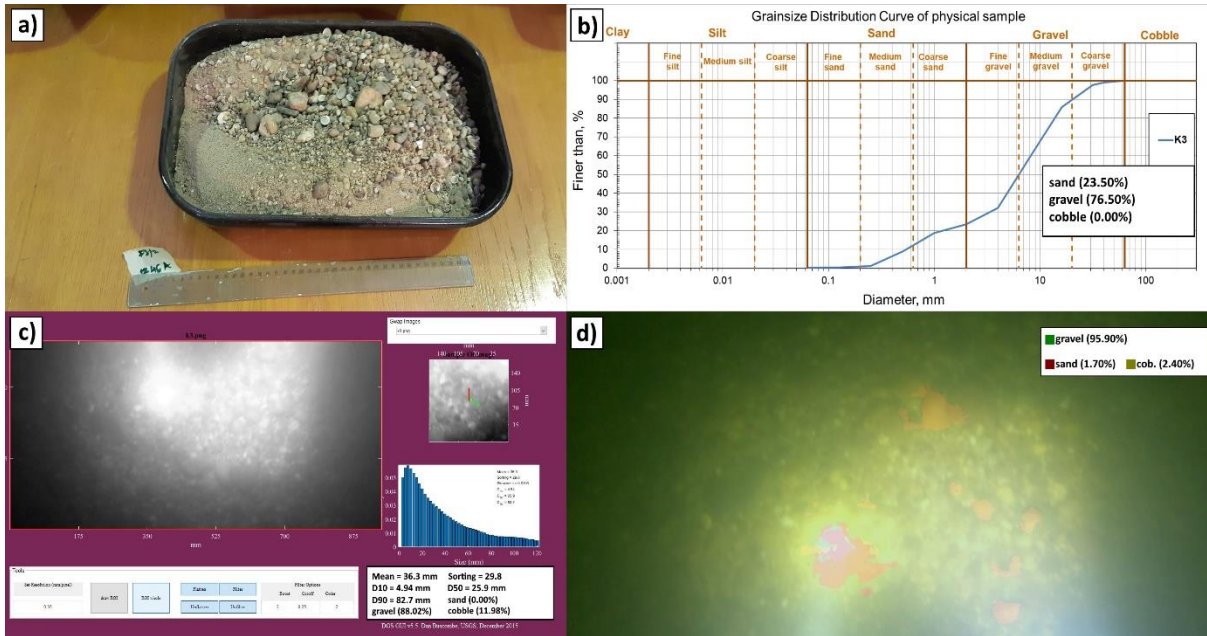
428 The AI result shows satisfactory match with the human evaluation. For example, around 100 m from the left bank,  
 429 between K1 and K2 sampling points, the AI peaks with around 70% sand and 30% gravel correctly. Furthermore,  
 430 on the two side of this peak a steep transition to gravel and decreasing sand occurs, similarly to the eye observation,  
 431 marked as sandy gravel and gravelly sand. Mixed sediment zones were also correctly identified by the AI at both  
 432 riverbanks.

433  
 434 Next, the AI estimated sediment classes were compared with both the physical samples and the wavelet method  
 435 at each sampling locations (Fig. 7). Overall, the AI based classification agrees well with the physical samples,  
 436 however, at sample K3 the ~20% sand content was neither reconstructed by the AI, nor could be observed by eye  
 437 in the images. Considering that the gravel dominates the bed sediments, the absence of sand fraction in the AI  
 438 results might be explained with the difference between the surface GSD and subsurface GSD. While both the AI  
 439 and the eye observation-based assessment focus on the bed surface, the physical sampling represents a thicker  
 440 layer, including the subsurface layer, too. Indeed, the so-called bed armouring phenomenon, taking place in the  
 441 vicinity of the thalweg in mixed-bed rivers, leads to coarser surface grains and finer subsurface grains (see e.g.,  
 442 Wilcock, 2005). This may also explain the case of K2 as it was located closer to the thalweg.

443 Fig. 10 presents an image of the collected physical sample in K3 together with its sieving result as well as the  
 444 underwater image of the riverbed surface in K3, and the results of the two different image processing methods.  
 445 Bed armouring is indeed present in the sampling point as the finer, sand fraction cannot be observed on the  
 446 riverbed surface, yet they appear in the collected bed material sample. In Fig. 11., supportive images of bed  
 447 armouring are provided, taken during our surveys in the Upper section of the Hungarian Danube. We broke the  
 448 surface armour to showcase the presence of the underlying finer fractions.

449





450  
451  
452  
453  
454

**Figure 10: Bed armour in sampling point K3. The measured percentages of fractions are also presented, respectively.**  
a) Image of the collected physical sample, containing both sand and gravel fractions. b) GSD curve of the physical sample, produced with sieving analysis. c) Wavelet analysis result of the image, taken in the sampling point. d) AI detection result in the sampling point.

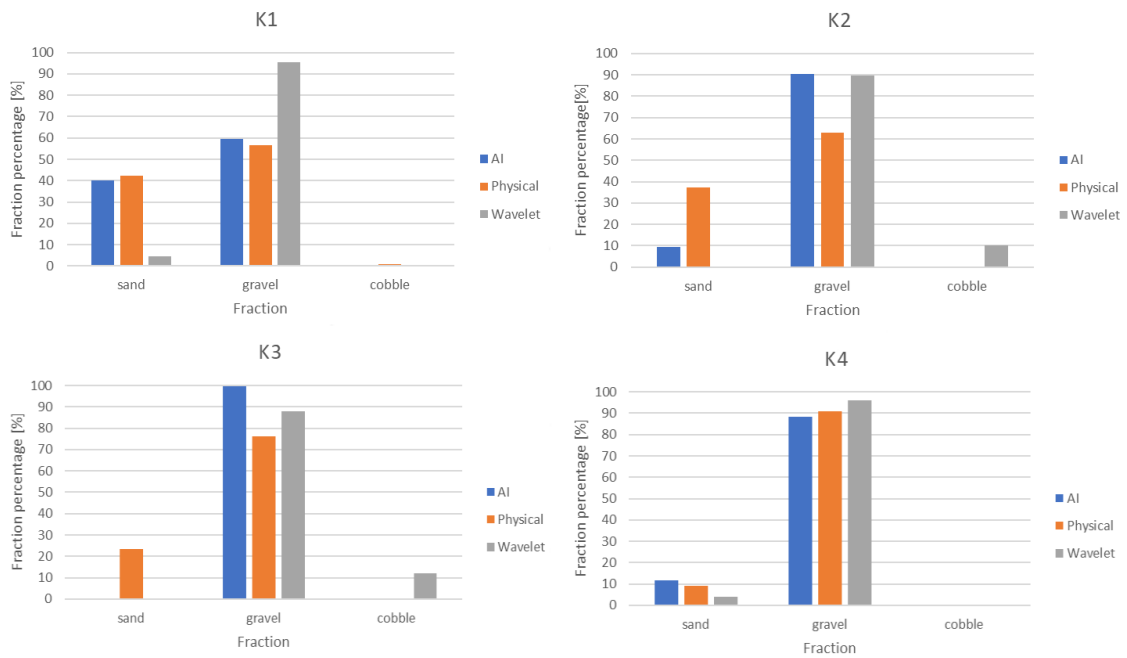
455



456

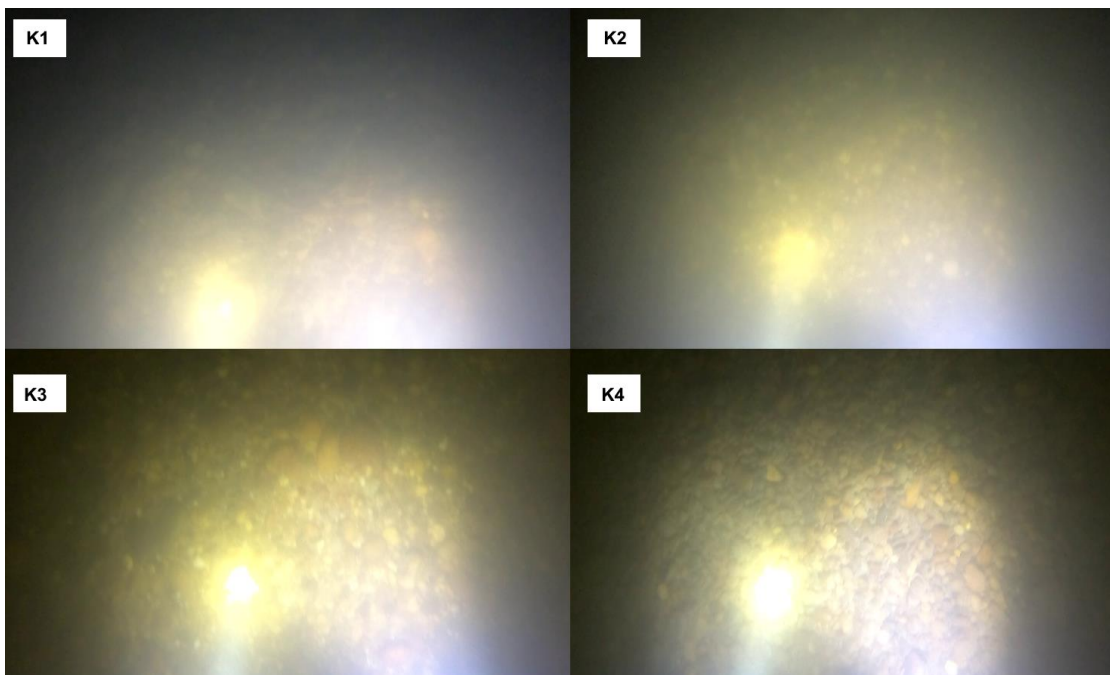
**Figure 11: Images of bed armoring, taken during our surveys in the Upper section of the Hungarian Danube.**

458 As for the wavelet analysis-based imagery technique, an overall slight overestimation of the coarse particles can  
459 be observed, and the sand classes are, in fact, not reconstructed correctly. This finding agrees well with the field  
460 experiences of Ermilov et al. (2020), where the authors indicated the strong sensitivity of the wavelet technique  
461 on the image resolution, and showed that to detect a grain, the diameter must be at least three times larger than  
462 the pixel. In this survey, the camera was indeed closer to the riverbed at sampling points K1 and K4 and the  
463 wavelet algorithm was able to detect coarse sand, but finer sand was neglected yielding the lower percentages,  
464 seen in Fig. 12.

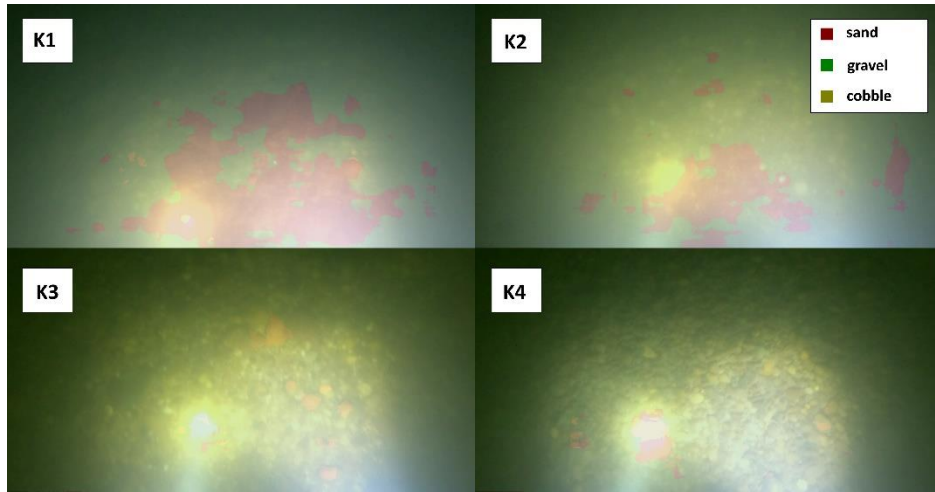


466  
 467 **Figure 12: Comparison of sediment fraction % at the sampling locations from the moving-averaged AI detection,**  
 468 **conventional sieving and the wavelet-based image processing method. Section A - II.**

469  
 470 The images of the bed from the sampling points are shown in Fig. 13, while Fig. 14 presents the AI detection  
 471 overlaid on these specific images, for visualisation purposes. As it was seen through the example of Fig. 8, a  
 472 moving-average has to be used for treating occurring noises. Hence, the AI results plotted in the bar- and smoothed  
 473 sectional plots are not necessarily representative of these instantaneous snapshots, such as Fig. 14.  
 474



475  
 476 **Figure 13: Riverbed video images at the sampling points in Section A - II.**



477

478 **Figure 14: Riverbed video images overlapped with their raw, AI detection result, at the sampling points in Section A -**  
 479 **II.**

480 At site B (Fig. 15) the river morphology is more complex compared to Site A as a groyne field is located along  
 481 the left bank (see again Fig. 2). As such, the low flow regions between the groynes yields the deposition of fine  
 482 sediments, and much coarser bed composition in the narrowed main stream. Even though no images containing  
 483 only fine sediments were applied in the training phase of the AI algorithm, the model still managed to successfully  
 484 distinguish these zones. The fine sediments in the deposition zone at the left bank was adequately estimated and  
 485 showed a good match with the visual evaluation for the whole cross-section (see Fig. 16).

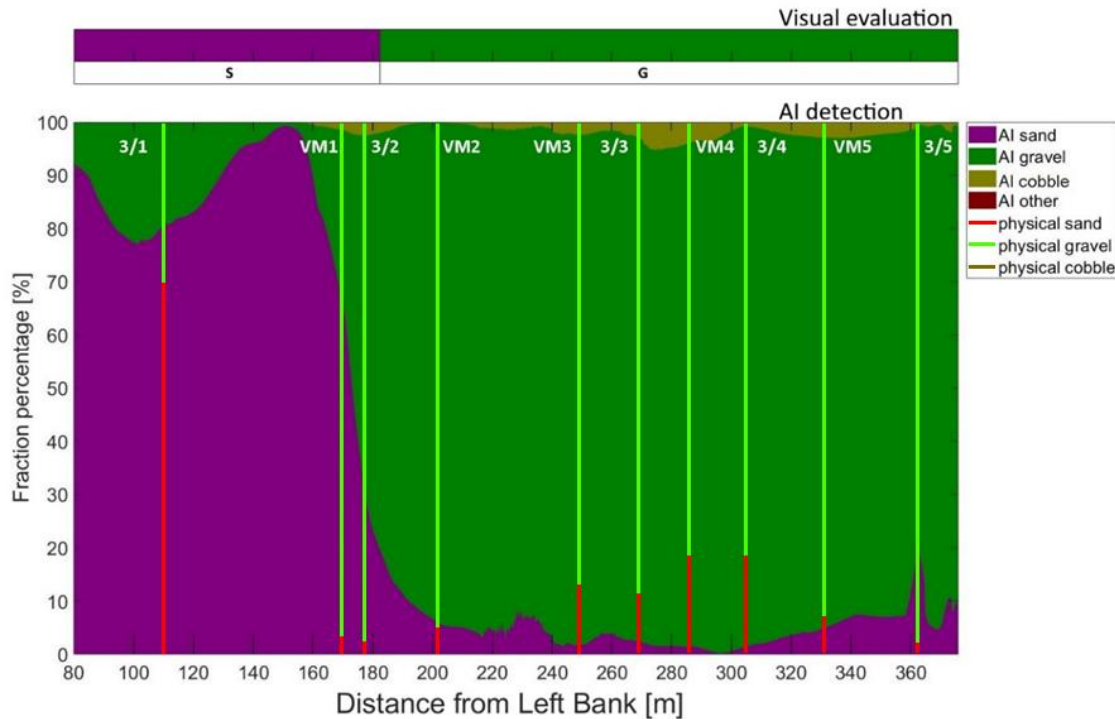
486



487 **Figure 15: The path of the vessel and camera in Section B - II, Site B. The polyline is coloured based on the sediment**  
 488 **seen during visual evaluation of the video. Yellow markers are the locations of physical bed material samplings. (Map**  
 489 **created with Google Earth Pro)**  
 490

491

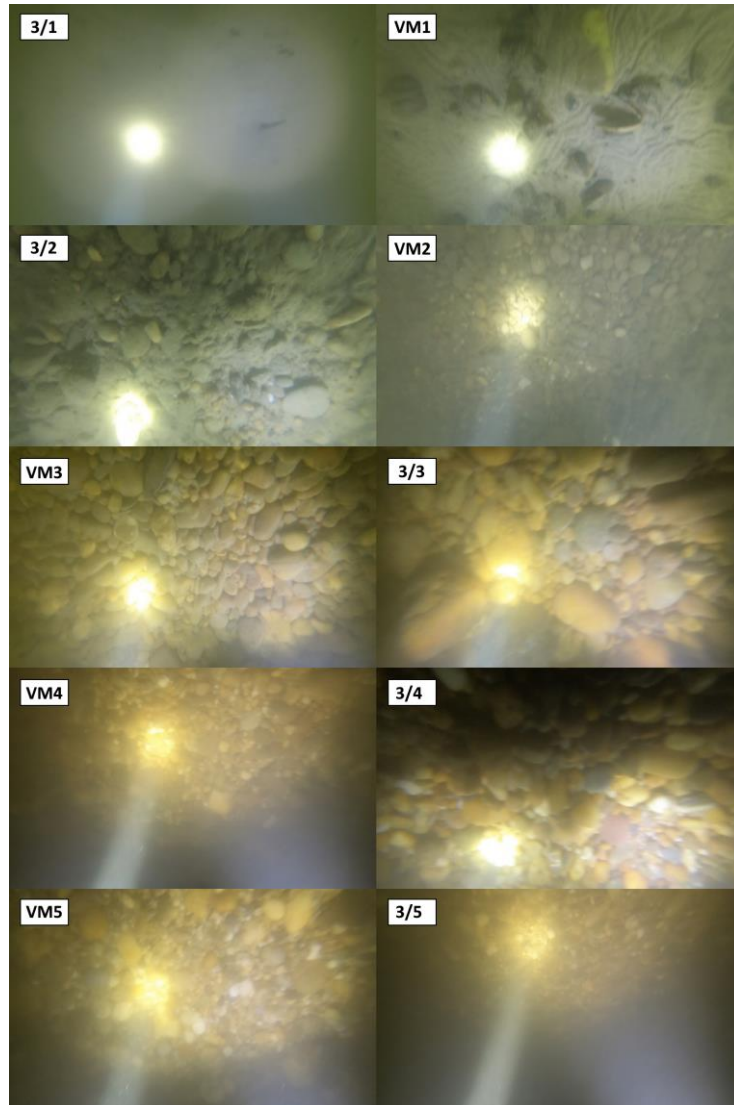




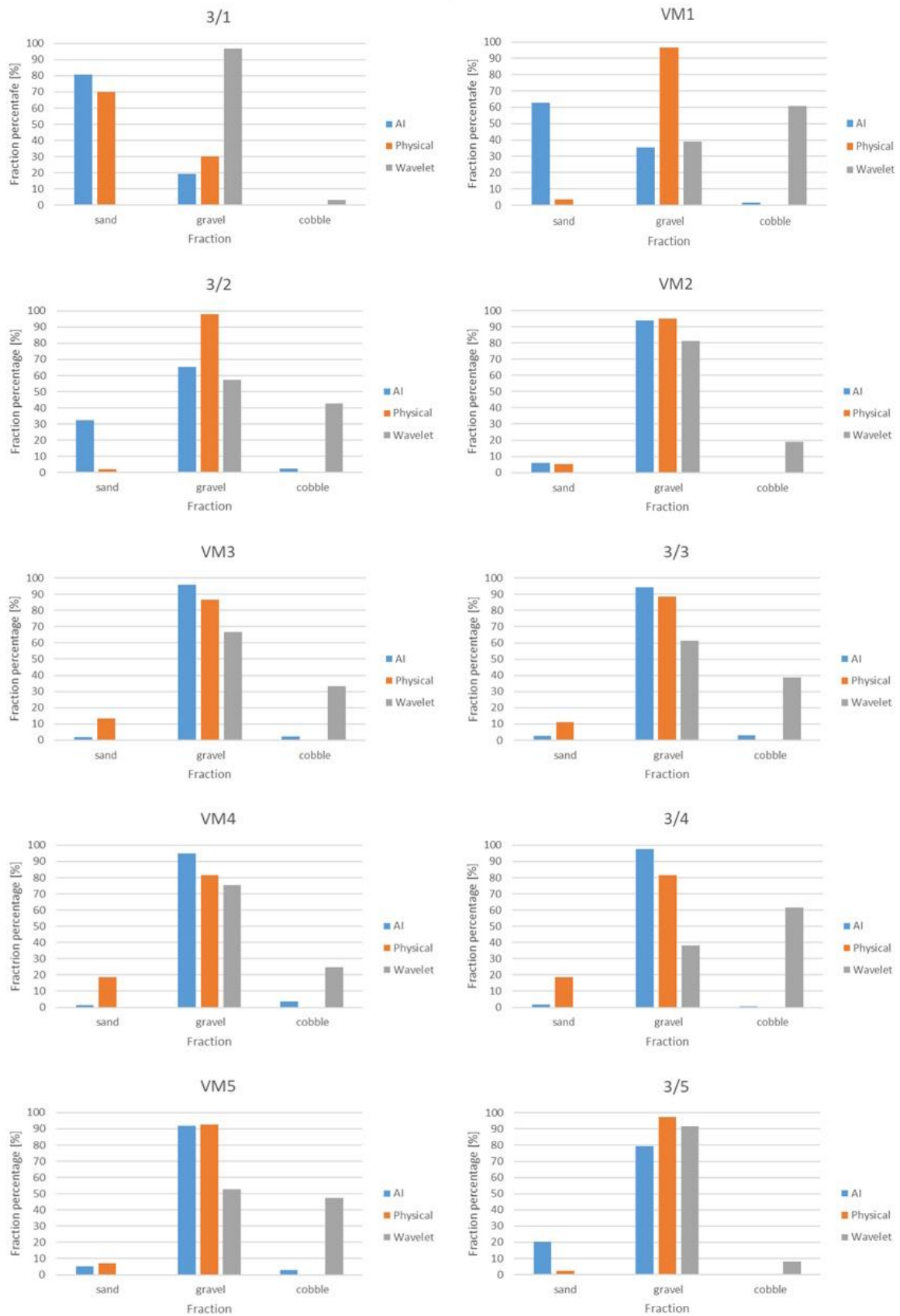
492  
 493 **Figure 16: Sediment fraction percentages in Section B - II, recognised by the AI. The visual evaluation included two**  
 494 **classes: gravel – G, sand – S). The fractions of the physical samples are shown as verticals.**

495  
 496 When comparing the AI results with the physical samples, the match is acceptable for most of the samples, such  
 497 as 3/1, VM2, VM3, 3/3, VM4, 3/4, VM5, respectively, with a highest difference of 10%. The significant  
 498 disagreements arose at sampling points VM1 and 3/2. Indeed, these points are located around the border of the  
 499 sediment deposition zone, showing steeply decreasing amount of sand moving away from the left bank (see the  
 500 variation from point 3/1 towards 3/2 in Fig. 17). This trend is successfully calculated by the AI algorithm, but the  
 501 physical samples for points VM1 and 3/2 show strong gravel dominance with negligible amount of sand (see Fig.  
 502 18). Resembling the findings at the other study site, this difference can likely be explained with the disturbed  
 503 physical samples, which contain the sediments of the subsurface layer, too. In this case, however, the fine sediment  
 504 layer is accumulated on the gravel particles. It is also worth noting that the physical samples are analysed by  
 505 weighing the different sediment size classes, resulting in weight distribution. On the other hand, the imagery  
 506 methods provide surface distributions, hence having a thin layer of fine sediments on the top can strongly bias the  
 507 resulted composition (Bunte and Abt, 2001; Sime and Ferguson, 2003; Rubin et al., 2007). In Fig. 19/a, the  
 508 grainsize frequency diagram (blue) showcases how the wavelet method incorrectly detected a gravel and a larger  
 509 cobble mode and it did not manage to identify sand. Again, this was due to not achieving the sufficient image  
 510 resolution required by the wavelet method. Fig. 19/b on the other hand presents the AI detection for the very same  
 511 image, with satisfactory results. The algorithm managed to segment the gravels and the sand patches.  
 512 At sampling point 3/5 a weaker, but still satisfactory agreement was found. Here, the AI indicated 20% sand in  
 513 contrast with the physical samples. Analysis of the raw videos may indicate that the suspended sediment  
 514 concentration was higher in this region and the transported fine particles frequently became visible passing  
 515 through the light beams, eventually causing disturbance in the AI analysis. Another issue in the AI algorithm was  
 516 associated with the illumination. Using a diving light with small beam divergence proved counterproductive. The

517 high intensity, focused light occasionally caused overexposed zones (white pixels) in the bed image, misleading  
518 the AI and resulting in detecting incorrect classes there. The use of wide beam divergence lamps is recommended  
519 instead, with uniform light. Examples for these problems are illustrated in Fig. 20 (a: overexposure, b: moving  
520 suspended sediment). Fig. 21 presents the AI detection overlaid on the images taken exactly in the sampling  
521 points.  
522

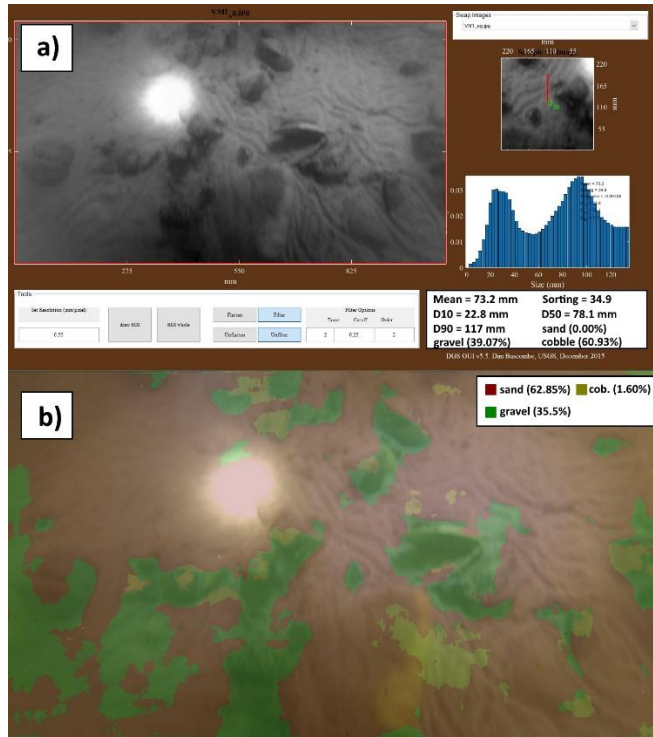


523  
524 **Figure 17: Riverbed video images at the sampling points in Section B - II.**



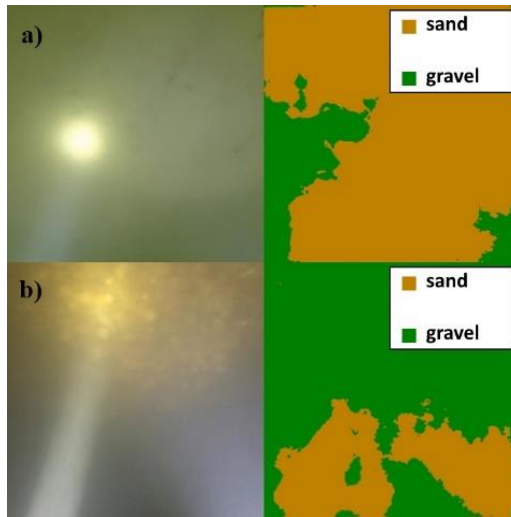
525  
526  
527

Figure 18: Comparison of sediment fraction % at the sampling locations from the moving-averaged AI detection, conventional sieving and the wavelet-based image processing method. Section B - II.



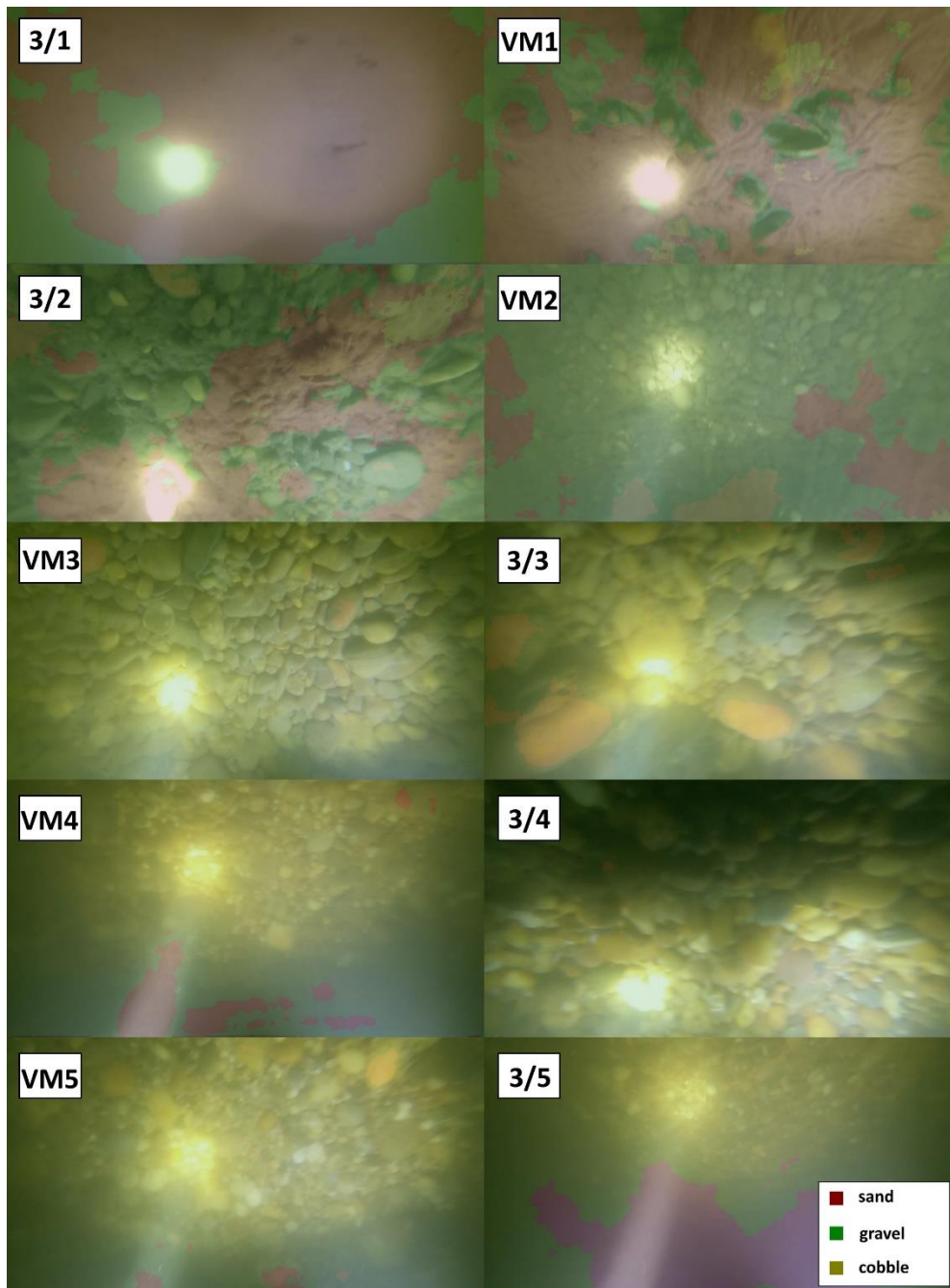
528  
529  
530

Figure 19: a) Wavelet analysis result of the underwater image in VM1. b) AI detection result of the same image.



531  
532  
533  
534

Figure 20: The effect of strong diving light on the AI algorithm in: a) purely sand covered zone and b) darker zone with higher SSC. The original images are on the left, while the AI detections can be found on the right.



535

536 **Figure 21: Riverbed video images overlapped with their raw, AI detection result, at the sampling points in Section B -**  
 537 **II.**

538

539 Results of the other measurements can be found in the Appendix. Fig. A2, B2 and C2 show that the trend of  
 540 riverbed composition from the visual evaluation is well-captured by the AI in the other cross-sections of the study  
 541 as well (see sampling points F/3, F/4, 1/1, 1/2 1/3, respectively). The resolution limit of the wavelet approach was  
 542 further noticeable (see Fig. A3, B3 and C3) as it was not able to detect sand, similarly to the sampling points  
 543 presented earlier. In Section A - III, traces of possible bed armouring were found as neither the eye observation  
 544 nor the AI detected sand class in the images (see Fig. B4) of F/1 and F/2, even though the physical samples  
 545 contained this fraction. In sampling point 1/4, the AI correctly detected the mixing of sand and gravel, but the  
 546 physical sample showed the dominance of sand rather than the gravel fraction (see Fig. C3). The possible

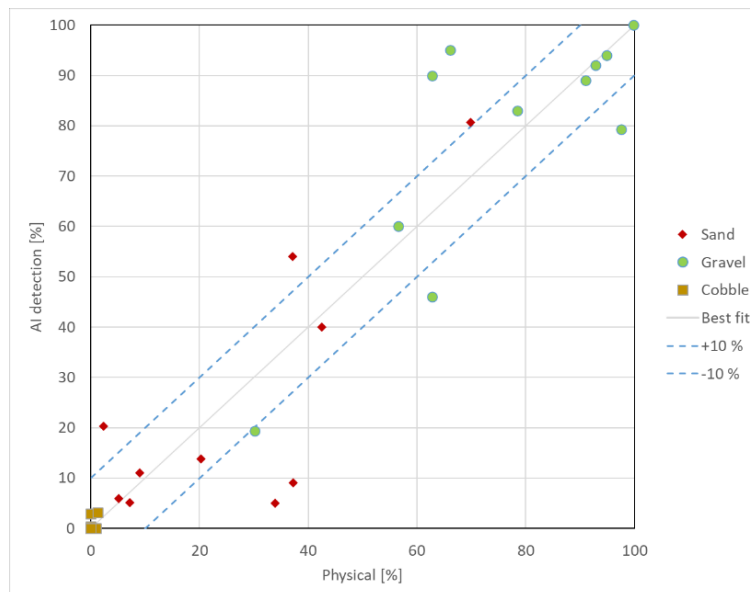


547 explanation behind these differences resembles what was the case for the K3 sampling point, introduced earlier:  
548 there was an additional finer fraction in the subsurface layer, hidden from the camera.

549

550 Finally, to quantify the efficiency of the introduced Deep Learning algorithm, we have selected the points which  
551 were determined to be the most comparable between the applied analysis methods. The decision was based on  
552 how well the given physical sample and riverbed image corresponded to each other. In the case of bad  
553 correspondence, the point was removed from the final comparison. These removed points belonged to one of the  
554 two scenarios that was discussed earlier: i) bed armouring, or ii) surface accumulation of a relatively thin sand  
555 layer, covering the gravel particles underneath. As a result, 11 points were kept and used for the final evaluation.  
556 These were: 1/1 from section B-I; 3/1, VM2, VM5, 3/5 from section B-II; F3, F4 from section A-I; K1, K2, K4  
557 from section A-II; and A5 from section A-III. Fig. 22 presents the AI-measured sediment fraction percentages  
558 against the data from their corresponding, sieved physical samples (i.e., the bar plots values, respectively). The  
559 differences between the AI and the physical samples for most of the points (7 out of 11) were less or equal to  
560 10%, while in the remaining 4 they did not exceed 20%.

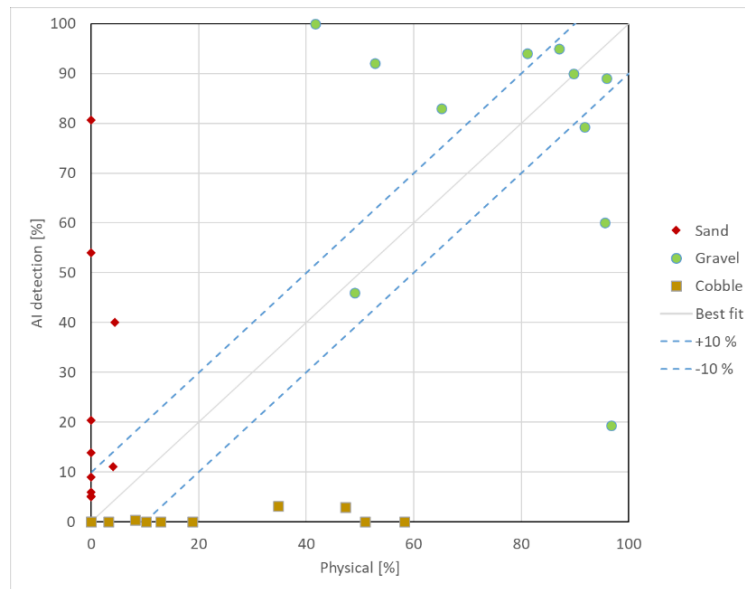
561



562  
563  
564

**Figure 22: Comparison of sediment fractions between the AI detection and physical samples, for the selected sampling points.**

565 Fig. 23 on the other hand compares the performance of the AI to the wavelet method. In this case, the discrepancies  
566 are greater, but this is due to the limitations of the wavelet approach, discussed earlier. For instance, the wavelet  
567 detected large amounts of cobbles in 4 points, while neither the AI, nor the physical samples (Fig. 22) did so.  
568 Furthermore, it was unable to recognise the sand fraction almost completely.



569

570 **Figure 23: Comparison of sediment fractions between the AI detection and the wavelet approach, for the selected**  
 571 **sampling points.**

572 Based on the results presented in this manuscript, it could be established that the AI managed to recognise the  
 573 main features of the riverbed material composition from underwater videos with satisfactory accuracy.

574 **4.3 Implementation challenges**

575 The power supply for the entire imaging infrastructure, i.e., for the camera, the diving lights and lasers, was  
 576 ensured by batteries. However, due to the low temperature at the river bottom, the battery level decreased  
 577 extremely fast, compared to normal circumstances. Providing the power supply directly from the motorboat  
 578 engines can overcome this issue. To keep the camera in the adequate height also caused difficulties, since getting  
 579 too close to the bed can harm the devices, lifting too high, on the other hand, will result in poor image quality.  
 580 The measured instantaneous ADCP flow depth data was used therefore to keep the bed in camera sight, while  
 581 maintaining proper boat velocity to avoid blurry images. Choosing a higher recording frequency, however, can be  
 582 beneficial and alter this limitation, when provided. Lower velocities could not be maintained as the river would  
 583 have moved the vessel out of the section. An alternative solution can be to move on longitudinal (streamline) paths  
 584 instead of transects. This would allow for lower vessel speed. This would increase the time of the measurement,  
 585 which still could be profitable if the images are of higher quality. However, the conventional way for river  
 586 bathymetry surveys is to move on transversal, cross-sectional paths, due to the river bathymetry having a lower  
 587 spatial variation along streamlines, compared to the changes that occur in the transversal direction (Benjankar et  
 588 al., 2015; Kinsman, 2015). As such, it may require carrying out a relatively dense set of longitudinal paths to gain  
 589 proper information, further increasing the time demand. Thus, for this alternative, higher attention needs to be  
 590 paid towards choosing these paths and the interpolation method. Another challenge can be the influence of drag  
 591 force on the measurement setup. In our case, even though the main body itself was a streamlined weight, equipping  
 592 the other tools on it turned the setup geometry irregular. Additionally, we found that our setup was a bit nose-  
 593 heavy. Due to this, and the drag force combined, the camera tilted forward during the measurements. As a result,  
 594 the lower parts of the raw images were sometimes too dark, as the camera was looking over the riverbed, and not  
 595 at the lit part of the bed. Examples for this could be seen in Fig. 17 (VM4, VM5, 3/5). Hence, in this manuscript

596 we decided to crop out the lower 25% of all raw images generally, before processing them to avoid this element  
597 of uncertainty. On the long term however, this effect could be reduced by building a streamlined container (e.g.,  
598 3D-printed body, or a body similar to unmanned underwater vehicles') with slots in it for each device, and also  
599 by improving the weight distribution. Furthermore, we hypothesize that by using lasers (as originally planned in  
600 this study) during the measurements, the known structure (i.e., the position and distances) of the laser points when  
601 the setup is perpendicular to the bed, can help to orthorectify the images. This will decrease the effect of occasional  
602 tilting when one wishes to carry out size analysis on the images. In our case, we presented how the wavelet method  
603 had inherently bigger issues (i.e., image resolution limit), which could not be caused by the camera tilting since  
604 those would be in a significantly lower magnitude of error.

605

606 As for the training of the AI algorithm with the underwater images, the illumination is indeed a more crucial  
607 aspect, compared to normal imagery methods. In many cases only the centre areas of the images were clearly  
608 visible, whereas the remaining parts were rather dark and shady. Determining the boundaries between distinct  
609 sediment classes for these images was challenging even for experienced eyes. This quality issue certainly  
610 generated some incorrect annotations. To overcome this issue, manually varying the white balance thus enhancing  
611 the visibility of the sediment could improve the training to some extent. It is worth noting that when Deep Learning  
612 methods are to be used, most of the problems arise from the data side (Yu et al., 2007), whereas issues related to  
613 the applied algorithms and hardware are rare. This is because data is more important from an accuracy perspective  
614 than the actual technical infrastructure (Chen et al., 2020). The time demand of image annotation (data  
615 preparation) is relatively high, i.e., a trained person could analyse roughly 10 images per hour. On the other hand,  
616 as introduced earlier, a great advantage of using AI is the capability of improving the quality of training itself,  
617 often yielding better agreement with reality, compared to the manual annotation. Similar results have been  
618 reported by Lu et al., (2018). This at the same time proves that with the introduced approach, there is no need for  
619 very precise manual training, thus a fast and effective training process can eventually be achieved.

620

621 The validation of the Deep Learning algorithm is far from straightforward. In this study, four approaches were  
622 adapted, i.e., a mathematical approach, and comparison with three other measurement methods, respectively. The  
623 mathematical approach was based on calculating pixel accuracy and the Intersection-over-union parameter, as it  
624 is usually done in case of Deep Learning methods to describe their efficiency (e.g., Rahman and Wang, 2016).  
625 However, the latter parameter was shown to be decreased even when the model improved. Consequently, using  
626 only the mathematical evaluation in this study could not describe adequately the model performance. Hence, the  
627 results were compared to those of three other methods: i) visual evaluation of the image series, ii) a wavelet-based  
628 image-processing method (using the method of Buscombe, 2013) and iii) riverbed composition data from physical  
629 samples. Considering the features of the applied methods, the first one, i.e., the visual observation, is expected to  
630 be the most suitable for the model validation. Indeed, when assessing the bed surface composition by eye, the  
631 same patterns are sought, i.e., both methods focus on the uppermost sediment layer. On the other hand, the physical  
632 sampling procedure inherently represents subsurface sediment layers, leading to different grain size distributions  
633 in many cases. For instance, as shown above, if bed armour develops in the riverbed and the sampler breaks-up  
634 this layer, the resulted sample can contain the finer particles from the subsurface layer. On the contrary, in zones  
635 where a fine sediment layer is deposited on coarse grains, i.e., a sand layer on the top of a gravel bed, the physical

636 samples represent the coarse material too, moreover, considering that the sieving provides weight distribution this  
637 sort of bias will even enhance the proportion of the coarse particles. Attempts were made to involve a third,  
638 wavelet-based method for model validation. However, this method failed when finer particles, i.e., sand,  
639 characterized the bed. This is an inherent limitation of these type of methods, as discussed earlier, i.e., the pixel  
640 size, is simply not fine enough to reconstruct the small grain diameters in the range below fine gravel. Lastly, the  
641 most suitable sample points were selected to quantify the performance of the AI. Holding the sieved physical  
642 samples as ground truth, the AI showed promising results. In 64% of the points, the difference between AI-  
643 detected and physical sediment percentages was less than or equal to 10%. In the rest, it did not surpassed 20%.

644

645 As it is known, the ML and DL models can learn unknown relationships in datasets, but unwanted biases as well.  
646 With our current dataset, in our opinion, these biases would be the darker tones of visible grain texture and the  
647 lack of larger grain sizes. This way our model in its current state is only applicable effectively in the chosen study  
648 site, until the dataset is not expanded with additional images from other rivers or regions. However, the purpose  
649 of the manuscript was to introduce the methodology itself and its potential in general and not to create a universal  
650 algorithm.

#### 651 **4.4 Novelty and future work**

652 The introduced image-based Deep Learning algorithm offers novel features in the field of sedimentation  
653 engineering. First, to the authors' knowledge, underwater images of the bed of a large river have not yet been  
654 analysed by AI. Second, the herein introduced method enables extensive (and still relatively quick) mapping of  
655 the riverbed, in contrast to most of the earlier approaches, where only several points or shorter sections were  
656 assessed with imagery methods. Third, the method is much faster compared to conventional samplings or non-AI  
657 based image-processing techniques. The field survey of a 400 m long transect took ~15 minutes, while the AI  
658 analysis took 4 minutes (approx. 7 image/s). The speed range of 0.2-0.45 m/s of the measurement vessel and the  
659 15 minutes per transect complies with the operating protocol of general ADCP surveys on rivers (e.g., RD  
660 Instruments, 1999; Simpson, 2002; Mueller and Wagner, 2013). Hence, the developed image-based measurement  
661 can be carried out together with the conventional boat-mounted ADCP measurements, further highlighting its time  
662 efficiency. Indeed, the method is a great alternative approach for assessing riverbed material on-the-go, in  
663 underwater circumstances. As an extensive and quick mapping tool, it can support other types of bed material  
664 samplings in choosing the sampling locations and their optimal number. Furthermore, it can be used for quickly  
665 detecting areas of sedimentation and their extent, as it was shown in Ch. 4.2. (Fig. 16). This way, it may support  
666 decisions regarding the maintenance of the channel or the bank-infiltrated drinking water production (detecting  
667 colmation and colmated zones). Fourth, a novel approach was used for the imaging and model training. As the  
668 camera-bed distance were constantly changing, the mm/pixel ratio also varied. Hence, no scale was defined for  
669 the algorithm beforehand. Earlier Deep Learning methods for sediment analysis all applied fixed camera heights  
670 and/or provided scaling for the AI. It should be noted that these were airborne measurements, mapping the dry  
671 zone of the rivers. In an underwater manner, it is extremely challenging to keep a fixed, constant camera height  
672 due to the spatially varying riverbed elevations. Hence, it is of major importance that this manuscript introduces  
673 a methodology and a Deep Learning algorithm which neglect the need for scaling. This way, the method is faster  
674 and easier to build, but also simpler to use. Of course, as a trade-off, the method, as of now, cannot reconstruct

675 detailed grainsize distributions. Indeed, the purpose was rather to provide a uniquely fast bed material mapping  
676 tool, additionally with a much denser spatial resolution than the conventional methods, saving up significant  
677 resources.

678

679 Originally, beside the three main sediment grain classes introduced in the manuscript (sand, gravel, cobble), others  
680 were also defined during annotation (e.g., bedrock, clams), but due to class imbalance (i.e., dominance of the three  
681 sediment classes), these were not adapted successfully. There is a good potential in improving the method through  
682 transfer learning (see Zamir et al., 2018) using broader dataset, involving other sediment types. Another possible  
683 way to counter imbalance is the use of so-called weighted cross entropy (see Lu et al., 2019) on the current dataset,  
684 which will also be investigated in our case.

685

686 Since the introduced method offers a quick way to provide extensive, spatially dense bed material information of  
687 its composition, it may be used to boost the training dataset of predictive, ensemble bagging-based Machine  
688 Learning techniques (e.g., Ren et al., 2020) and improve their accuracy. Furthermore, the method can support the  
689 implementation of other imagery techniques. For instance, using one of the training videos of this study the authors  
690 managed to reconstruct the grain-scale 3D model of a riverbed section with the Structure-from-Motion technique  
691 (Ermilov et al., 2020), enabling the quantitative estimation of surface roughness. Underwater field cameras can  
692 also be used for monitoring and estimating bedload transport rate (Ermilov et al., 2022) by adapting LS-PIV and  
693 the Statistical Background Model approach. This latter videography technique may also be used with moving  
694 cameras (e.g., Hayman and Ekhlund, 2003), which enables its adaptation into our method by e.g., detecting  
695 bedload movement in the cross-section.

696

697 The statistical representativity of the introduced method, as a surface sampling technique, needs to be also  
698 addressed in future work. Following and building upon the experience of conventional, surface sampling  
699 procedures (e.g., grid sampling; Diplas, 1988) may prove to be beneficial, where they provided the exact number  
700 of gravel particles needed to be included (Wolman, 1954) to satisfy the representativity criteria. Then, using edge-  
701 and blob-detection would enable to calculate and compare the number of gravel particles in the images to this  
702 value. Furthermore, we intend to apply 2 cameras, with overlapping FOVs for increasing the covered area (and  
703 the representativity) during surveys. Besides, it would also improve the accuracy of the Structure-from-Motion  
704 technique mentioned earlier.

## 705 **5 Conclusion**

706 A novel, artificial intelligence-based riverbed sediment analysis method has been introduced in this manuscript,  
707 which uses underwater images to reconstruct the spatial variation of the characteristic sediment classes. The  
708 method was trained and validated with a reasonably high number (~15000) of images, collected in a large river,  
709 in the Hungarian section of the Danube. The main novelties of the developed Deep Learning based procedure are  
710 the followings: i) underwater images are used, ii) the method enables mapping of the riverbed along the  
711 measurement vessel's route with very dense spatial allocation, iii) cost-efficient, iv) works without scaling, i.e.,  
712 the distance between the camera and the riverbed can vary. Consequently, in contrast with conventional pointwise  
713 bed sediment analysis methods, this technique is robust and capable of providing continuous sediment

714 composition data covering whole river reaches, eventually providing the possibility to set up 2D bed material  
715 maps. In this way, river reach scale hydromorphological assessments can be supported, where the composition of  
716 bed surface is of interest, e.g., when performing habitat studies, parameterising 2D and 3D computational  
717 hydrodynamic and morphodynamic models, or assessing the impact of restoration measures.

718 **Financial support.** The first author acknowledges the support of the ÚNKP-21-3 New National Excellence  
719 Programme of the Ministry for Innovation and Technology, and the National Research, Development and  
720 Innovation Fund, Hungary.

721 **Code availability.** The code written and used in this manuscript is available here: [https://bmeedu-](https://bmeedu-my.sharepoint.com/:f:/g/personal/ermilov_alexander_emk_bme_hu/EjI2neM4AOZGsBkYgKReViEBBzRFRFoYyLlmo6SzTB_qDQ?e=AqpqHI)  
722 [my.sharepoint.com/:f:/g/personal/ermilov\\_alexander\\_emk\\_bme\\_hu/EjI2neM4AOZGsBkYgKReViEBBzRFRFo](https://bmeedu-my.sharepoint.com/:f:/g/personal/ermilov_alexander_emk_bme_hu/EjI2neM4AOZGsBkYgKReViEBBzRFRFoYyLlmo6SzTB_qDQ?e=AqpqHI)  
723 [YyLlmo6SzTB\\_qDQ?e=AqpqHI](https://bmeedu-my.sharepoint.com/:f:/g/personal/ermilov_alexander_emk_bme_hu/EjI2neM4AOZGsBkYgKReViEBBzRFRFoYyLlmo6SzTB_qDQ?e=AqpqHI)

724 **Data availability.** The dataset and results can be accessed using the following link: [https://bmeedu-](https://bmeedu-my.sharepoint.com/:f:/g/personal/ermilov_alexander_emk_bme_hu/EhoGx64sP1tFnj8Z1OdMZAsBZWd5gDYzPyodSUDdWFjeiw?e=hKIXjq)  
725 [my.sharepoint.com/:f:/g/personal/ermilov\\_alexander\\_emk\\_bme\\_hu/EhoGx64sP1tFnj8Z1OdMZAsBZWd5gDY](https://bmeedu-my.sharepoint.com/:f:/g/personal/ermilov_alexander_emk_bme_hu/EhoGx64sP1tFnj8Z1OdMZAsBZWd5gDYzPyodSUDdWFjeiw?e=hKIXjq)  
726 [zPyodSUDdWFjeiw?e=hKIXjq](https://bmeedu-my.sharepoint.com/:f:/g/personal/ermilov_alexander_emk_bme_hu/EhoGx64sP1tFnj8Z1OdMZAsBZWd5gDYzPyodSUDdWFjeiw?e=hKIXjq)

727 **Author contributions.** GB developed the code and carried out the training process. AAE carried out the  
728 fieldwork, evaluated the results, did the laboratory analysis, and collaborated with GB in improving the images.  
729 SB oversaw and directed the project, while managing the financial- and equipment background.

730 **Competing interest.** The contact author has declared that none of the authors has any competing interest.

731 **Acknowledgements.** The authors would like to thank our students Dávid Koós, Gergely Tikász, Schrott Márton  
732 and our technicians István Galgóczy, István Pozsgai, Károly Tóth and András Rehák for fieldwork support.

## 733 References

734 Adams, J.: Gravel Size Analysis from Photographs. J. Hydraul. Div., 1979, 105, 1247–1255.  
735 doi/10.1061/JYCEAJ.0005283, 1979.

736  
737 Anglin, D. R., Haeseker, S. L., Skalicky, J. J., Schaller, H., Tiffan, K. F., Hatten, J. R., et al.: Effects of Hydropower  
738 Operations on Spawning Habitat, Rearing Habitat, and Standing/Entrapment Mortality of Fall Chinook Salmon  
739 in the Hanford Reach of the Columbia River. US Fish and Wildlife Service, final Report. Available at:  
740 <https://pubs.er.usgs.gov/publication/70179516>, 2006.

741  
742 Baranya, S., Fleit, G., Józsa, J., Szalóky, Z., Tóth, B., Czeglédi, I. and Erős, T.: Habitat mapping of riverine fish  
743 by means of hydromorphological tools. Ecohydrology, Volume 11, Issue 7 e2009. Available at:  
744 <https://doi.org/10.1002/eco.2009>, 2018.

745  
746 Barnard, P., Rubin, D., Harney, J. and Mustain, N.: Field test comparison of an autocorrelation technique for  
747 determining grain size using a digital beachball camera versus traditional methods. Sedimentary Geology, 201(1–  
748 2): 180–195., 2007.

749  
750 Benjankar, R., Tonina, D., Mckean, J.: One-dimensional and two-dimensional hydrodynamic modelling derived  
751 flow properties: Impacts on aquatic habitat quality predictions. Earth Surf. Process. Landf. 2015, 40, 340–356.  
752

753 Benkő, G., Baranya, S., Török, T. G., and Molnár, B.: Folyami mederanyag szemösszetételének vizsgálata Mély  
754 Tanulás eljárással drónfelvételek alapján (in English: Analysis of composition of riverbed material with Deep  
755 Learning based on drone video footages). *Hidrológiai Közlöny*, 100, 61–69., 2020. Manuscript  
756 Breheret, A.: Pixel Annotation Tool. Av. at: <https://github.com/abreheret/PixelAnnotationTool>, 2017.  
757  
758 Bunte, K. and Abt, S. R.: Sampling Surface and Subsurface Particle-Size Distributions in Wadable Gravel- and  
759 Cobble-Bed Streams for Analyses in Sediment Transport, Hydraulics, and Streambed Monitoring; General  
760 Technical Report (GTR), U.S. Department of Agriculture, Forest Service, Rocky Mountain Research Station: Fort  
761 Collins, CO, USA, 2001.  
762  
763  
764 Buscombe, D. and Masselink, G.: Grain size information from the statistical properties of digital images of  
765 sediment. *Sedimentology*, 56, 421–438. doi/10.1111/j.1365-3091.2008.00977.x, 2008.  
766  
767 Buscombe, D.: Transferable wavelet method for grain-size distribution from images of sediment surfaces and thin  
768 sections, and other natural granular patterns. *Sedimentology*, 60 1709–1732., 2013.  
769  
770 Buscombe, D., Grams, P. and Kaplinski, M.: Characterizing riverbed sediment using high-frequency acoustics: 1.  
771 Spectral properties of scattering. *Journal of Geophysical Research: Earth Surface*, doi: 10.1002/2014JF003189,  
772 119:12, (2674-2691), 2014a.  
773  
774 Buscombe, D., Grams, P. and Kaplinski, M.: Characterizing riverbed sediment using high-frequency acoustics: 2.  
775 Scattering signatures of Colorado Riverbed sediment in Marble and Grand Canyons. *Journal of Geophysical  
776 Research: Earth Surface*, doi/full/10.1002/2014JF003191, 119:12, (2674-2691), 2014b.  
777  
778 Buscombe, D. and Ritchie, A. C.: Landscape Classification with Deep Neural Networks. *Geosciences*, 8, 244.  
779 Available at: <https://doi.org/10.3390/geosciences8070244> , 2018.  
780  
781 Buscombe, D.: SediNet: a configurable deep learning model for mixed qualitative and quantitative optical  
782 granulometry optical granulometry. *Earth Surface Processes and Landforms*, 45, 638-651. DOI:  
783 10.1002/esp.4760, 2020.  
784  
785  
786 Chandler, J., Lane, S. N. and Ashmore, P.: Measuring river-bed and flume morphology and parameterising bed  
787 roughness with a KODAK DCS460 digital camera. *International Archives of Photogrammetry and Remote  
788 Sensing*, Vol. XXXIII, Part B7., 2000.  
789  
790 Chen, C., Zhang, P., Zhang, H., Dai, J., Yi, Y., Zhang, H. and Zhang, Y.: Deep Learning on Computational-  
791 Resource-Limited Platforms: A Survey. Volume 2020, Article ID 8454327. Available at:  
792 <https://doi.org/10.1155/2020/8454327>, 2020.  
793  
794 Chen, L., Zhu, Y., Isola, P., Papandreou, G., Schroff, F. and Adam, H.: Encoder-Decoder with Atrous Separable  
795 Convolution for Semantic Image Segmentation. *Proceedings of the European conference on computer vision  
796 (ECCV)* (pp. 801-818). <https://arxiv.org/abs/1802.02611>., 2018.  
797  
798 Cheng, D., Li, X., Li, W. H., Lu, C., Li, F., Zhao, H. and Zheng, W. S.: Large-Scale Visible Watermark Detection  
799 and Removal with Deep Convolutional Networks. In book: *Pattern Recognition and Computer Vision. First  
800 Chinese Conference, PRCV, Guangzhou, China, Proceedings, Part III*. DOI: 10.1007/978-3-030-03338-5\_3,  
801 2018.  
802  
803 Cheng, Z., and Liu, H.: Digital grain-size analysis based on autocorrelation algorithm. *Sedimentary Geology*, 327,  
804 21-31. Available at: <https://doi.org/10.1016/j.sedgeo.2015.07.008>, 2015.  
805  
806 Chezar, H. and Rubin, D. M.: Underwater Microscope System. United States Patent Office, The United States of  
807 America as represented by the Secretary of the Interior, US Patent No. 6,680,795 B2., 2004.  
808  
809 Church, M. A., McLean, D. G., and Wolcott, J. F.: Sediments transport in Gravel Bed Rivers. Chap.: *Riverbed  
810 Gravels: Sampling and Analysis*. John Wiley and Sons, New York, 43–88, 1987.  
811

812 Delong, M. D. and Brusven, M. A.: Classification and spatial mapping of riparian habitat with applications toward  
813 management of streams impacted by nonpoint source pollution. *Environmental Management*, 15:565-571. DOI:  
814 10.1007/BF02394745, 1991.

815

816 Detert, M. and Weitbrecht, V.: User guide to gravelometric image analysis by BASEGRAIN. In *Advances in*  
817 *Science and Research*; Fukuoka, S., Nakagawa, H., Sumi, T., Zhang, H., Eds.; Taylor and Francis Group: London,  
818 UK, 2013; pp. 1789–1795. ISBN 978-1-138-00062-9., 2013.

819

820 Diplas, P.: Sampling Techniques for Gravel Sized Sediments. *Journal of Hydraulic Engineering*. DOI:  
821 10.1061/(ASCE)0733-9429(1988)114:5(484), 1988.

822

823 Ermilov, A.A., Baranya, S. and Török, G.T.: Image-Based Bed Material Mapping of a Large River. *Water*, 12,  
824 916. Available at: <https://doi.org/10.3390/w12030916>, 2020.

825

826 Ermilov, A. A., Fleit, G., Conevski, S., Guerrero, M., Baranya, S., & Rütther, N.: Bedload transport analysis using  
827 image processing techniques. *ACTA GEOPHYSICA*, 1895-6572 1895-7455. [http://doi.org/10.1007/s11600-022-](http://doi.org/10.1007/s11600-022-00791-x)  
828 00791-x, 2022.

829

830 Fehr, R.: Einfache Bestimmung der Korngrößenverteilung von Geschiebematerial mit Hilfe der  
831 Linienzahlanalyse (In English: Simple detection of grain size distribution of sediment material using line-count  
832 analysis). *Schweizer Ing. und Archit.*, 105, 1104–1109., 1987.

833

834 Ferdowski, B., Ortiz, C. P., Houssais, M., & Jerolmack, D. J. (2017). Riverbed armouring as a granular segregation  
835 phenomenon. *Nature Communications* 2017 8:1, 8(1), 1–10. <https://doi.org/10.1038/s41467-017-01681-3>  
836

837 Fetzer, J., Holzner, M., Plötze, M. and Furrer, G.: Clogging of an Alpine streambed by silt-sized particles –  
838 Insights from laboratory and field experiments. *Water Research*, Volume 126, Pages 60-69.  
839 <https://doi.org/10.1016/j.watres.2017.09.015>, 2017.

840

841 Geist, D. R., Jones, J., Murray, C. J. and Dauble, D. D.: Suitability criteria analyzed at the spatial scale of redd  
842 clusters improved estimates of fall chinook salmon (*Oncorhynchus tshawytscha*) spawning habitat use in the  
843 Hanford Reach, Columbia River. *Canadian Journal of Fisheries and Aquatic Sciences*, 57: 1636-1646., 2000.

844

845 Gilcher, M. and Udelhoven, T.: Field Geometry and the Spatial and Temporal Generalization of Crop  
846 Classification Algorithms—A Randomized Approach to Compare Pixel Based and Convolution Based Methods.  
847 *Remote Sens.*, 13, 775., 2021.

848

849 GOPRO Hero 4 Silver: User Manual. Available at: [https://gopro.com/content/dam/help/hero4-](https://gopro.com/content/dam/help/hero4-silver/manuals/UM_H4Silver_ENG_REVA_WEB.pdf)  
850 [silver/manuals/UM\\_H4Silver\\_ENG\\_REVA\\_WEB.pdf](https://gopro.com/content/dam/help/hero4-silver/manuals/UM_H4Silver_ENG_REVA_WEB.pdf), 2014.

851

852 GOPRO Hero 7 Black: User Manual. Available at: [https://gopro.com/content/dam/help/hero7-](https://gopro.com/content/dam/help/hero7-black/manuals/HERO7Black_UM_ENG_REVA.pdf)  
853 [black/manuals/HERO7Black\\_UM\\_ENG\\_REVA.pdf](https://gopro.com/content/dam/help/hero7-black/manuals/HERO7Black_UM_ENG_REVA.pdf), 2018.

854

855 Graham, D. J., Reid, I. and Rice, S. P.: Automated sizing of coarse-grained sediments: image-processing  
856 procedures. *Mathematical Geology*, 37, 1–28. <https://doi.org/10.1007/s11004-005-8745-x>, 2005.

857

858 Graham, D. J. Rollet, A.J., Piégay, H. and Rice, S. P.: Maximizing the accuracy of image-based surface sediment  
859 sampling techniques. *Water Resour. Res.*, 46, W02508. [https://doi.org/](https://doi.org/10.1029/2008WR006940)  
860 [10.1029/2008WR006940](https://doi.org/10.1029/2008WR006940), 2010.

861

862 Grams, P. E., Topping, D. J., Schmidt, J. C., Hazel, J. E. and Kaplinski, M.: Linking morphodynamic response  
863 with sediment mass balance on the Colorado River in Marble Canyon: Issues of scale, geomorphic setting, and  
864 sampling design, *J. Geophys. Res. Earth Surf.*, 118, 361–381, doi:10.1002/jgrf.20050., 2013.

865

866 Guerit, L., Barrier, L., Liu, Y., Narteau, C., Lajeunesse, E., Gayer, E., Métivier, F.: Uniform grain-size distribution  
867 in the active layer of a shallow, gravel-bedded, braided river (the Urumqi River, China) and implications for paleo-  
868 hydrology. *Earth Surface Dynamics*. 6. 1011-1021. DOI: 10.5194/esurf-6-1011-2018., 2018.

869



870 Guerrero, M., Rüther, N., Szupiany, R., Haun, S., Baranya, S. and Latosinski, F.: The Acoustic Properties of  
871 Suspended Sediment in Large Rivers: Consequences on ADCP Methods Applicability. *Water*, 8, 13;  
872 doi:10.3390/w8010013, 2016.

873

874 Haddadchi, A., Booker, D.J. and Measures, R.J.: Predicting riverbed substrate cover proportions across New  
875 Zealand. *Catena*, Volume 163, pp. 130-146. Available at: <https://doi.org/10.1016/j.catena.2017.12.014>, 2018.

876

877 Hayman, E., Eklundh, J.: Statistical Background Subtraction for a Mobile Observer. Proceedings of the Ninth  
878 IEEE International Conference on Computer Vision (ICCV 2003) 2-Volume Set 0-7695-1950-4/03, 2003.

879

880 He, F., Liu, T., Tao, D.: Control batch size and learning rate to generalize well: theoretical and empirical evidence.  
881 *Neural Information Processing Systems*, 2019.

882

883 Ibbeken, H., and Schleyer, R.: Photo-sieving: A method for grain-size analysis of coarse-grained, unconsolidated  
884 bedding surfaces. *Earth Surf. Process. Landforms*, 11, 59-77. Available at:  
885 <https://doi.org/10.1002/esp.3290110108>, 1986.

886

887 Igethinathane, C., Melin, S., Sokhansanj, S., Bi, X., Lim, C. J., Pordesimo, L. O. and Columbus, E. P.: Machine  
888 vision based particle size and size distribution determination of airborne dust particles of wood and bark pellets.  
889 *Powder Technol.*, 196, 202-212. Available at: <https://doi.org/10.1016/j.powtec.2009.07.024>, 2009.

890

891 Kellerhals, R. and Bray, D. I.: Sampling Procedures for Coarse Fluvial Sediments. *J. Hydraul. Div.*, 97, 1165-  
892 1180., 1971.

893

894 Kim, H., Han, J. and Han, T. Y.: Machine vision-driven automatic recognition of particle size and morphology in  
895 SEM images. *Nanoscale*, 12, 19461-19469. Available at: <https://doi.org/10.1039/D0NR04140H>, 2020.

896

897 Kinsman, N.: Single-Beam Bathymetry Data Collected in Shallow-Water Areas near Gambell, Golovin, Hooper  
898 Bay, Savoonga, Shishmaref, and Wales, Alaska 2012-2013; Department of Natural Resources. Division of  
899 Geological & Geophysical Surveys: Fairbanks, AK, USA, 2015.

900

901 Le, Q. V.: Building high-level features using large scale unsupervised learning. In Proceedings of the 2013 IEEE  
902 International Conference on Acoustics, Speech and Signal Processing, Vancouver, BC, Canada, pp. 8595-8598.,  
903 2013.

904

905 Leopold, L. B.: An Improved Method for Size Distribution of Stream Bed Gravel. *Water Resour. Res.*, 6, 1357-  
906 1366. <https://doi.org/10.1029/WR006i005p01357>, 1970.

907

908 Limare, A., Tal, M., Reitz, M. D., Lajeunesse, E., and Métivier, F.: Optical method for measuring bed topography  
909 and flow depth in an experimental flume. *Solid Earth*, 2, 143-154, <https://doi.org/10.5194/se-2-143-2011>., 2011.

910

911 Lowe, D. G.: Distinctive Image Features from Scale-Invariant Keypoints. *International Journal of Computer  
912 Vision*, 60, pages 91-110, 2004.

913

914 Lu, S., Gao, F., Piao, Ch. and Ma, Y.: Dynamic Weighted Cross Entropy for Semantic Segmentation with  
915 Extremely Imbalanced Data. 2019 International Conference on Artificial Intelligence and Advanced  
916 Manufacturing (AIAM). doi: 10.1109/AIAM48774.2019.00053, 2019.

917

918 Mueller D. S., Wagner, Ch. R.: Measuring Discharge with Acoustic Doppler Current Profilers from a Moving  
919 Boat. USGS, Chapter 22 of Book 3, Section A. <https://pubs.usgs.gov/tm/3a22/>, 2009.

920

921 Mueller D. S., Wagner, Ch. R.: Measuring discharge with acoustic Doppler current profilers from a moving boat,  
922 version 2.0. [https://www.researchgate.net/publication/284587353\\_Measuring\\_discharge\\_with\\_acoustic\\_-\\_Doppler\\_current\\_profilers\\_from\\_a\\_moving\\_boat](https://www.researchgate.net/publication/284587353_Measuring_discharge_with_acoustic_-_Doppler_current_profilers_from_a_moving_boat), 2013.

923

924

925 Muste, M., Baranya, S., Tsubaki, R., Kim, D., Ho, H., Tsai, H. and Law, D.: Acoustic mapping velocimetry. *Water  
926 Resour. Res.*, 52, 4132-4150, doi:10.1002/2015WR018354., 2016.

927

928 Obodovskiy, O., Habel, M., Szatten, D., Rozlach, Z., Babiński, Z., Maerker, M.: Assessment of the Dnieper  
929 Alluvial Riverbed Stability Affected by Intervention Discharge Downstream of Kaniv Dam. *Water*, 12(4):1104.  
930 <https://doi.org/10.3390/w12041104>, 2020.  
931  
932 Padilla, R., Netto, S. M. and da Silva, E. A. B.: A Survey on Performance Metrics for Object-Detection  
933 Algorithms. Conference: 2020 International Conference on Systems, Signals and Image Processing (IWSSIP).  
934 DOI: 10.1109/IWSSIP48289.2020, 2020.  
935  
936 Perez, L. and Wang, J.: The Effectiveness of Data Augmentation in Image Classification using Deep Learning.  
937 arXiv preprint arXiv:1712.04621. Av. at: <https://arxiv.org/abs/1712.04621>, 2017.  
938  
939 Purinton, B. and Bookhagen, B.: Introducing PebbleCounts: A grain-sizing tool for photo surveys of dynamic  
940 gravel-bed rivers. *Earth Surf. Dyn.*, 7, 859–877. <https://doi.org/10.5194/esurf-7-859-2019>, 2019.  
941  
942 Rákóczi, L.: Selective erosion of noncohesive bed materials. *Geografiska Annaler. Series A, Physical Geography*,  
943 Vol. 69, No. 1, pp. 29-35. <https://doi.org/10.2307/521364>, 1987.  
944  
945 Rákóczi, L.: Identification of river channel areas inclined for colmation, based on the analysis of bed material.  
946 *Vízügyi Közlemények, LXXIX.*, chapter 3., 1997.  
947  
948 Rahman, M. A. and Wang, Y.: Optimizing Intersection-Over-Union in Deep Neural Networks for Image  
949 Segmentation. In: Bebis G. et al. (eds) *Advances in Visual Computing. ISVC 2016. Lecture Notes in Computer*  
950 *Science*, vol 10072. Springer, Cham. [https://doi.org/10.1007/978-3-319-50835-1\\_22](https://doi.org/10.1007/978-3-319-50835-1_22), 2016.  
951  
952 RD Instruments – Acoustic Doppler Current Profilers – Application Note: [https://www.commtec.com/library/Technical\\_Manuscripts/RDI/FSA-004%20Model1.pdf](https://www.commtec.com/library/Technical_Manuscripts/RDI/FSA-004%20Model1.pdf), 1999.  
953  
954  
955 Rice, S. and Church, M.: Grain size along two gravel-bed rivers: Statistical variation, spatial pattern and  
956 sedimentary links. *Earth Surf. Process. Landf.*, 23, 345–363., 1998.  
957  
958 Ren, H., Hou, Z., Duan, Z., Song, X., Perkins, W.A., Richmond, M. C., Arntzen, E. V. and Scheibe, T. D.: Spatial  
959 Mapping of Riverbed Grain-Size Distribution Using Machine Learning. *Front. Water*, 2:551627. doi:  
960 10.3389/frwa.2020.551627, 2020.  
961  
962 Rozniak, A., Schindler, K., Wegner, J. D. and Lang, N.: Drone images and Deep Learning for river monitoring in  
963 Switzerland. Semester project. Institute of Geodesy and Photogrammetry, Project, Swiss Federal Institute of  
964 Technology (ETH) Zurich, 2019.  
965  
966 Rubin, D. M.: A simple autocorrelation algorithm for determining grain-size from digital images of sediment. *J.*  
967 *Sed. Res.*, 74, 160–165., 2004.  
968  
969 Rubin, D. M., Chezar, H., Harney, J. N., Topping, D. J., Melis, T. S., Sherwood, C. R.: Underwater microscope  
970 for measuring spatial and temporal changes in bed-sediment grain size. *Sedimentary Geology*, Volume 202, Issue  
971 3, Pages 402-408, <https://doi.org/10.1016/j.sedgeo.2007.03.020>, 2007.  
972  
973 Scheder, C., Lerchegger, B., Flödl, P., Csar, D., Gumpinger, C. and Hauer, C.: Riverbed stability versus clogged  
974 interstitial: Depth-dependent accumulation of substances in freshwater pearl mussel (*Margaritifera margaritifera*  
975 L.) habitats in Austrian streams as a function of hydromorphological parameters. *Limnologica*, Volume 50,  
976 January 2015, Pages 29-39. <https://doi.org/10.1016/j.limno.2014.08.003>, 2015.  
977  
978 Shields, F. D., Jr. and Rigby, J. R.: River habitat quality from river velocities measured using acoustic Doppler  
979 current profiler. *Environ. Manage.*; 36(4):565-75. doi: 10.1007/s00267-004-0292-6., 2005.  
980  
981 Shields, F. D. Jr.: Aquatic Habitat Bottom Classification Using ADCP. *Journal of Hydraulic Engineering*, Vol.  
982 136, Issue 5, 2010.  
983  
984 Sime, L. C. and Ferguson, R. I.: Information on grain-sizes in gravel bed rivers by automated image analysis. *J.*  
985 *Sed. Res.*, 73, 630–636., 2003.  
986

987 Simpson, M. R.: Discharge Measurements Using a Broad-Band Acoustic Doppler Current Profiler. USGS, Open-  
988 File Report 01-1, <https://pubs.usgs.gov/of/2001/ofr0101/>, 2002.  
989

990 Singer, M. B.: A new sampler for extracting bed material sediment from sand and gravel beds in navigable rivers.  
991 Earth Surface Processes and Landforms 33(14):2277 – 2284 DOI: 10.1002/esp.1661, 2008.  
992

993 Soloy, A., Turki, I., Fournier, M., Costa, S., Peuziat, B. and Lecoq, N.: A Deep Learning-Based Method for  
994 Quantifying and Mapping the Grain Size on Pebble Beaches. Remote Sens., 12, 3659, doi:10.3390/rs12213659,  
995 2020.  
996

997 Staudt, F., Mullarney, J. C, Pilditch, C. A. and Huhn, K.: Effects of grain-size distribution and shape on sediment  
998 bed stability, near-bed flow and bed microstructure. Earth Surface Processes and Landforms, 44(5). DOI:  
999 10.1002/esp.4559, 2018.  
1000

1001 Sun, Z., Zheng, H. and Sun, L.: Analysis on the Characteristics of Bed Materials in the Jinghong Reservoir on the  
1002 Lancang River. Sustainability, 13, 6874. <https://doi.org/10.3390/su13126874>, 2021.  
1003

1004 Takechi, H., Aragaki, S. and Irie, M.: Differentiation of River Sediments Fractions in UAV Aerial Images by  
1005 Convolution Neural Network. Remote Sens., 13, 3188. <https://doi.org/10.3390/rs13163188>, 2021.  
1006

1007 Taravat, A., Wagner, M. P., Bonifacio, R. and Petit, D.: Advanced Fully Convolutional Networks for Agricultural  
1008 Field Boundary Detection. Remote Sens., 13, 722., 2021.  
1009

1010 Török, G. T., Baranya, S. (2017) Morphological Investigation of a Critical Reach of the Upper Hungarian Danube.  
1011 Periodica Polytechnica Civil Engineering. 61(4), pp. 752–761. <https://doi.org/10.3311/PPci.10530>, 2017.  
1012

1013 USDA: Guidelines for Sampling Bed Material. Technical Supplement 13A, 2007.  
1014

1015 Vanoni, V. A. and Hwang, L. S.: Relation between Bed Forms and Friction in Streams. J. Hydraulics Division.,  
1016 93 (3), 121–144. doi:10.1061/JYCEAJ.0001607, 1967.  
1017

1018 Verdú, J. M., Batalla, R. J. and Martínez-Casanovas, J. A.: High-resolution grain-size characterisation of gravel  
1019 bars using imagery analysis and geo-statistics. Geomorphology, 72, 73–93., 2005.  
1020

1021 Warrick, J. A., Rubin, D. M., Ruggiero, P., Harney, J. N., Draut, A. E. and Buscombe, D.: Cobble cam: Grain-  
1022 size measurements of sand to boulder from digital photographs and autocorrelation analyses. Earth Surf. Process  
1023 Landf., 34, 1811–1821. <https://doi.org/10.1002/esp.1877>, 2009.  
1024

1025 Wilcock, P. R.: Persistence of armor layers in gravel-bed streams. Hydrology and Land Surface Studies.  
1026 <https://doi.org/10.1029/2004GL021772>, 2005.  
1027

1028 Wolcott, J. F., Church, M.: Strategies for sampling spatially heterogeneous phenomena: The example of river  
1029 gravels. Journal of Sedimentary Research. v. 61, no. 4, p. 534–543, 1991.  
1030

1031 Wolman, M. G.: Method of sampling coarse river bed material. Trans. Am., Geophysical Union, 35(6), 951-956.  
1032

1033 WMO: Measurement of river sediments: prepared by the Rapporteur on Sediment Transport of the Commission  
1034 for Hydrology. Report, World Meteorological Organization - No. 561, Operational hydrology report (OHR)- No.  
1035 16, 1981.  
1036

1037 Yang, F., Yi, M., Cai, Y., Blasch, E., Sullivan, N., Sheaff, C., Chen, G. and Ling, H.: Multitask Assessment of  
1038 Roads and Vehicles Network (MARVN). Proceedings Volume 10641, Sensors and Systems for Space  
1039 Applications XI, 106410D, <https://doi.org/10.1117/12.2305972>, 2018.  
1040

1041 You, K., Long, M., Wang, J., Jordan M.I.: How Does Learning Rate Decay Help Modern Neural Networks?  
1042 <https://doi.org/10.48550/arXiv.1908.01878>, 2019.  
1043

1044 Yu, L., Wang, S. and Lai, K.K.: Data Preparation in Neural Network Data Analysis. In book: Foreign-Exchange-  
1045 Rate Forecasting with Artificial Neural Networks. DOI: 10.1007/978-0-387-71720-3\_3, 2007.  
1046

- 1047 Zamir, A. R., Sax, A., Shen, W., Guibas, L., Malik, J. and Savarese, S.: Taskonomy: Disentangling Task Transfer  
1048 Learning. In Proceedings of the 2018 IEEE/CVF Conf. on Computer Vision and Pattern Recognition, Salt Lake  
1049 City, UT, USA, pp. 3712–3722. doi: 10.1109/CVPR.2018.00391, 2018.  
1050
- 1051 Zhang, Q., Shi, Y., Chen, Z. and Jiang, T.: ADCP measured flow current of the middle-lower Changjiang River  
1052 channel. *Front. Earth Sci., China* 2, 1–9. <https://doi.org/10.1007/s11707-008-0016-y>, 2008.  
1053
- 1054 Zhou, Y., Lu, J., Jin, Z., Li, Y., Gao, Y., Liu, Y. and Chen, P.: Experimental Study on the Riverbed Coarsening  
1055 Process and Changes in the Flow Structure and Resistance in the Gravel Riverbed Downstream of Dams. *Front.*  
1056 *Environ. Sci.*, <https://doi.org/10.3389/fenvs.2021.611668>, 2021.  
1057
- 1058 Zhu, J., Park, T., Isola, P. and Efros, A. A.: Unpaired Image-to-Image Translation using Cycle-Consistent  
1059 Adversarial Networks. arxiv, <https://arxiv.org/abs/1703.10593>, 2020.  
1060

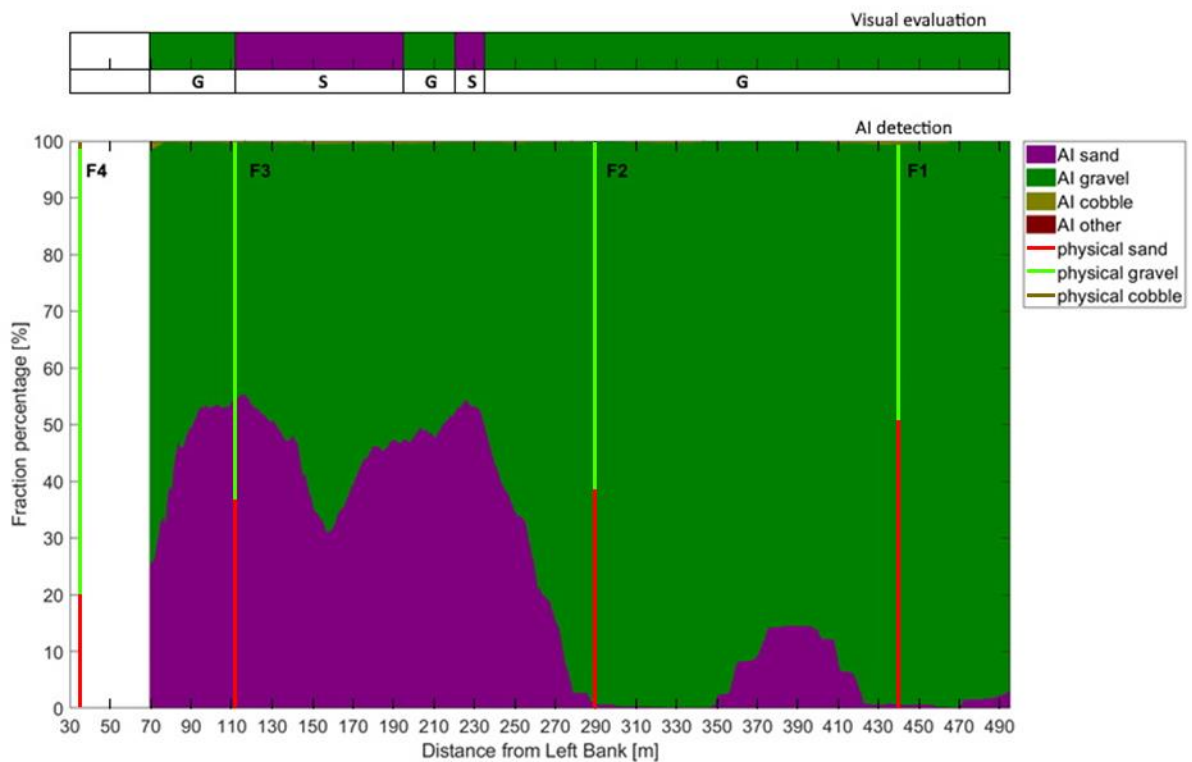
1061 Appendix

1062 Appendix A Site A - Section A - I



1063 Figure A1: The path of the vessel and camera in Section A - I, Site A. The polyline is coloured based on the sediment  
1064 seen during visual evaluation of the video. Yellow markers are the locations of physical bed material samplings. (Map  
1065 created with Google Earth Pro)  
1066

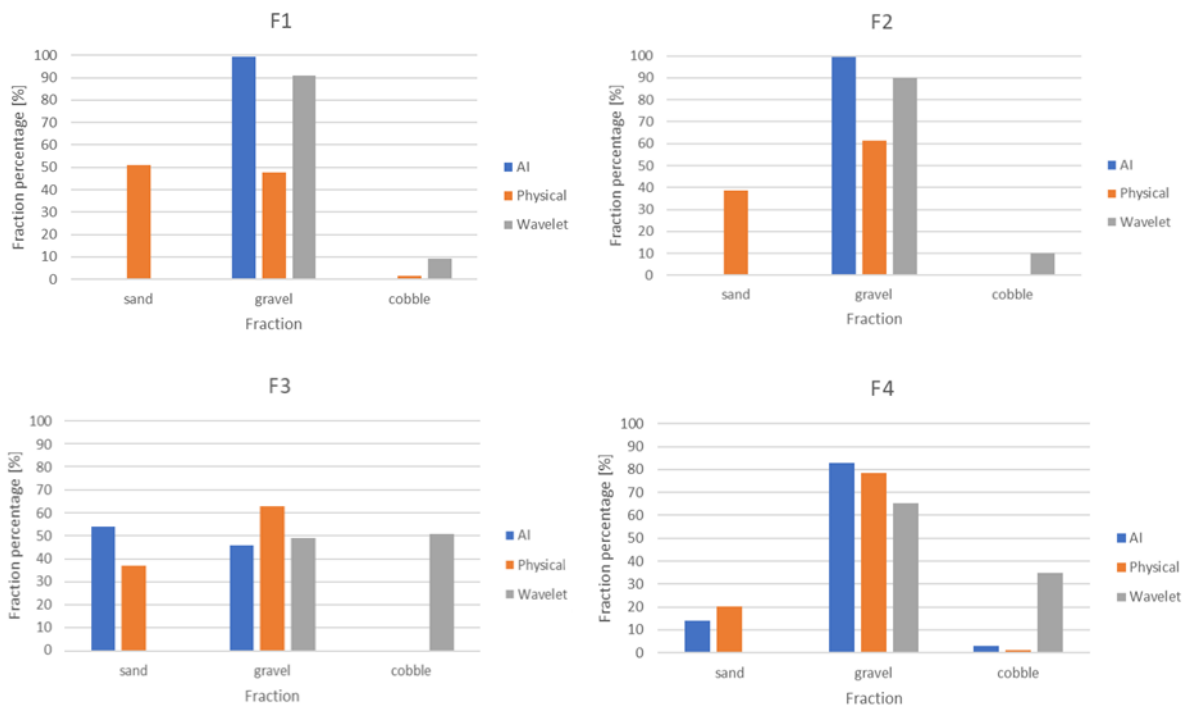
1067



1068 Figure A2: Sediment fraction percentages in Section A - I, recognised by the AI. The visual evaluation included two  
1069 classes: gravel – G, sand – S). The fractions of the physical samples are shown as verticals.  
1070

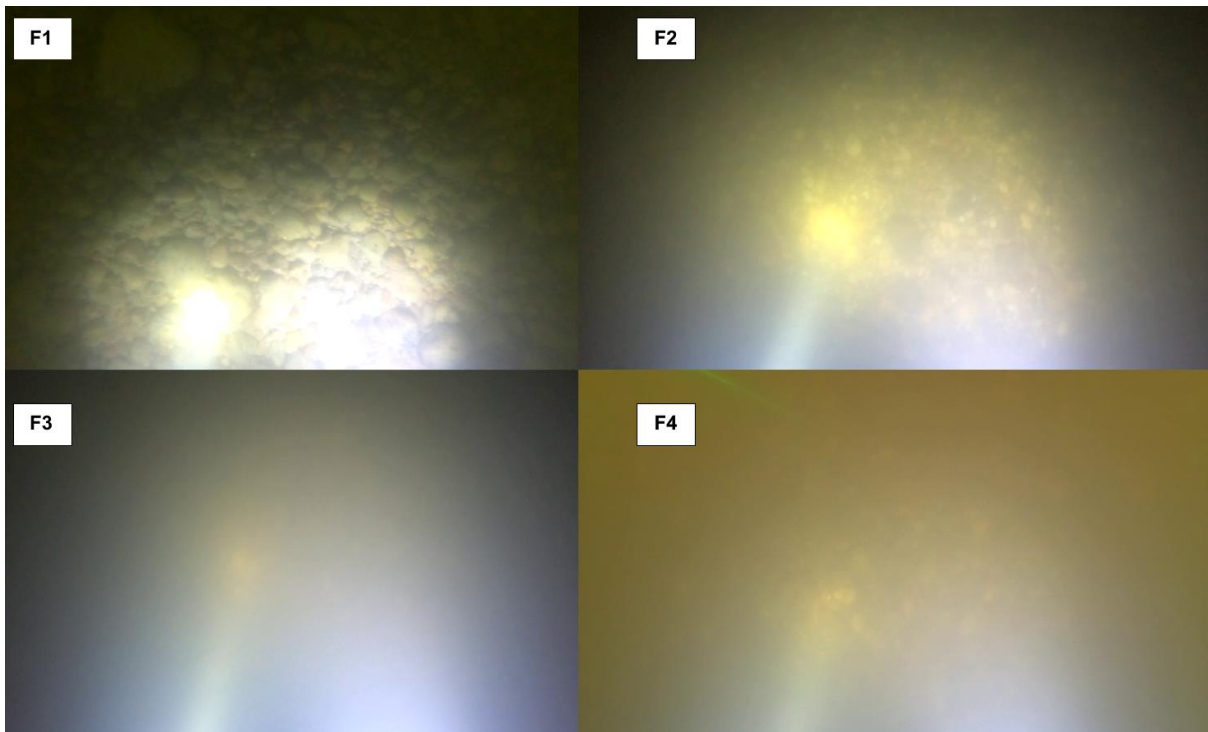


1071



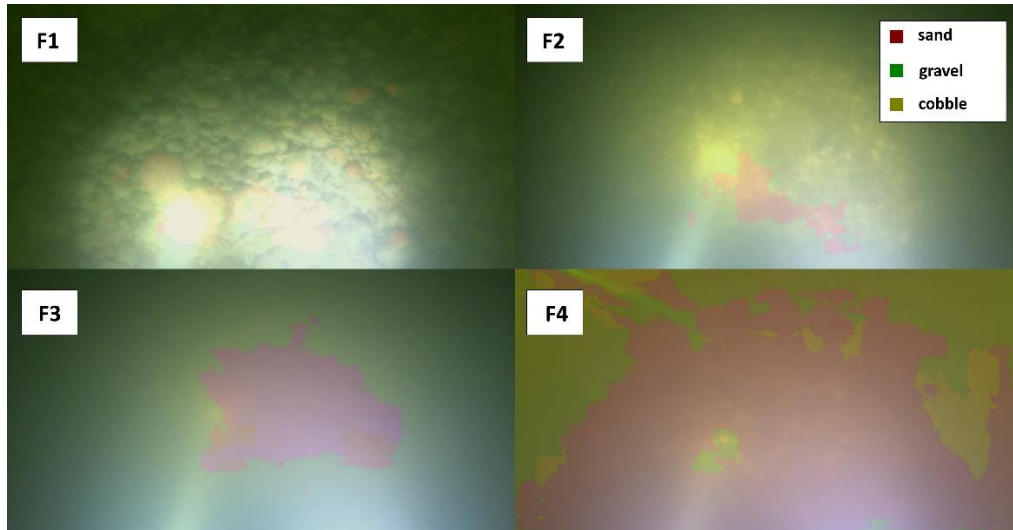
1072  
1073  
1074

Figure A3: Comparison of sediment fraction % at the sampling locations from the moving-averaged AI detection, conventional sieving and the wavelet-based image processing method. Section A - I.



1075  
1076  
1077

Figure A4: Riverbed video images at the sampling points in Section A - I.



1078

1079  
1080

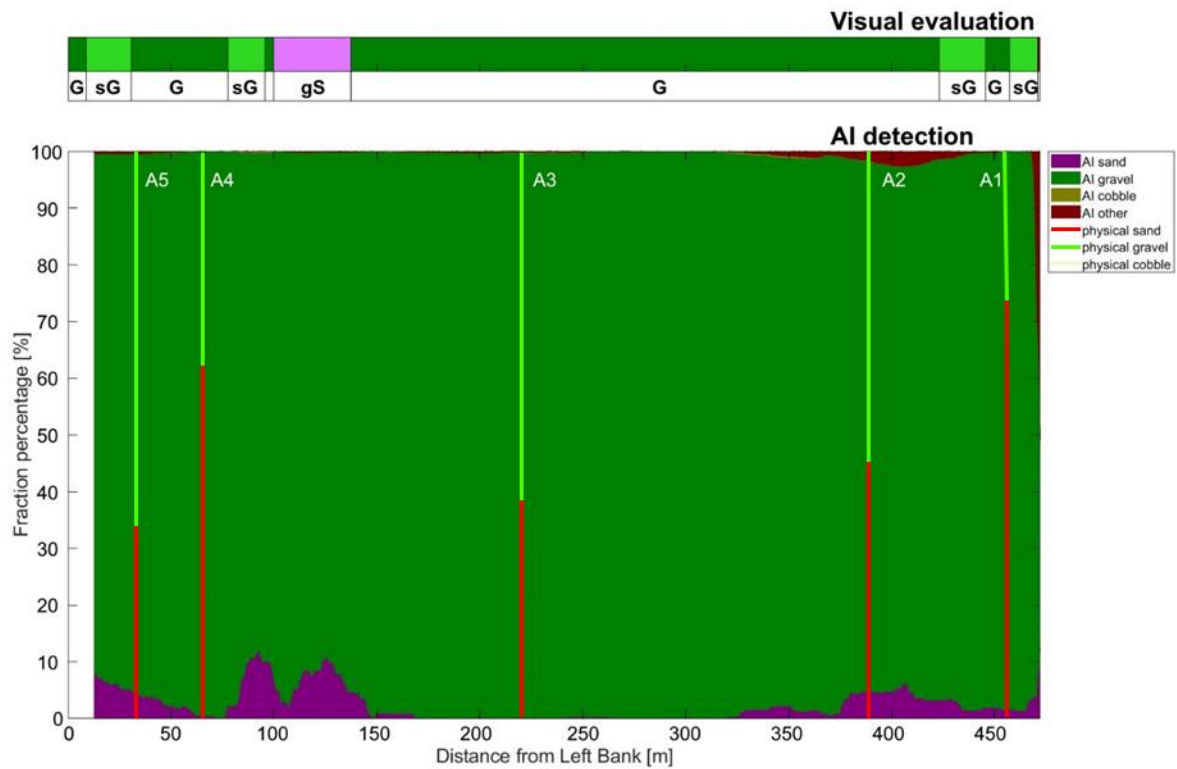
Figure A5: Riverbed video images overlapped with their raw, AI detection result, at the sampling points in Section A - I.

1081 Appendix B Site A – Section A - III



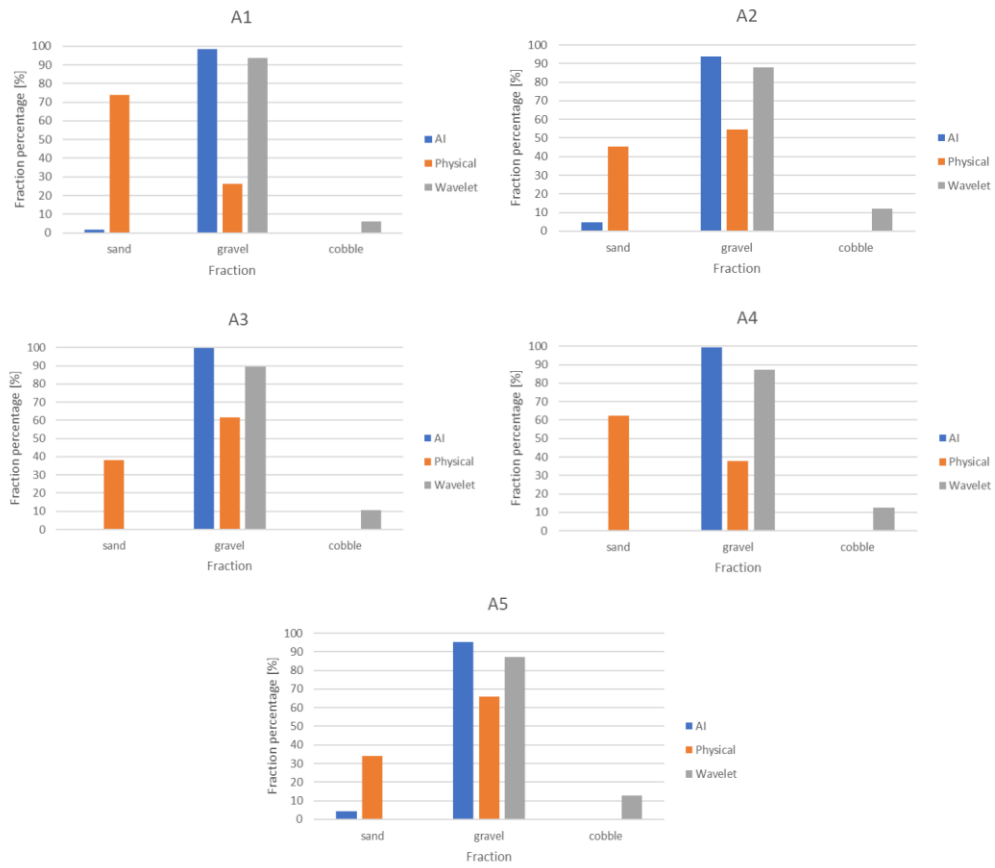
1082  
1083 **Figure B1: The path of the vessel and camera in Section A - III, Site A. The polyline is coloured based on the sediment**  
1084 **seen during visual evaluation of the video. Yellow markers are the locations of physical bed material samplings. (Map**  
1085 **created with Google Earth Pro)**

1086



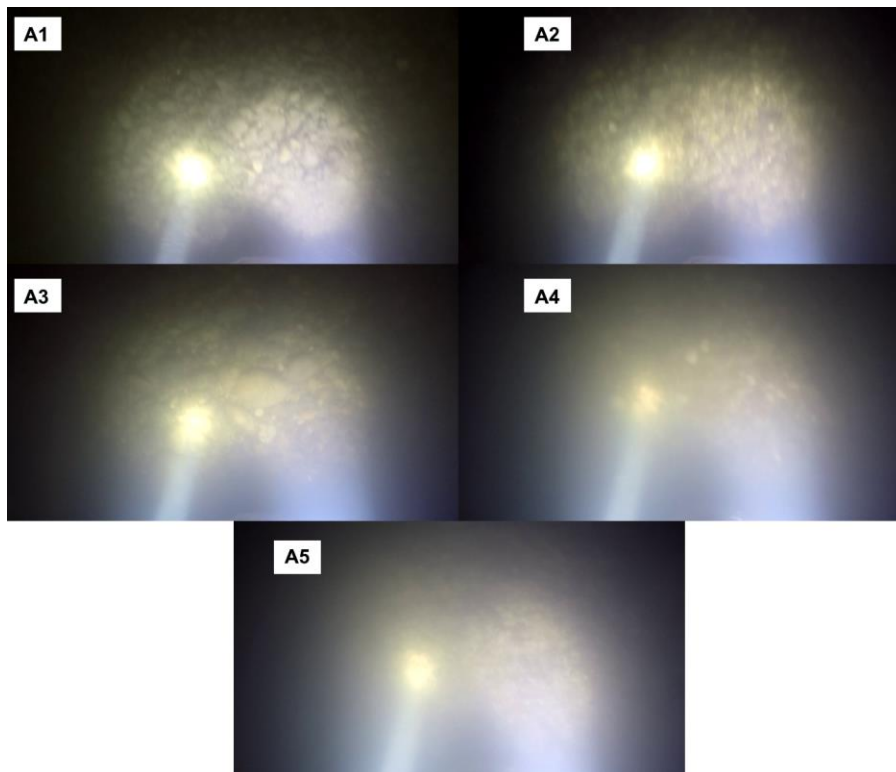
1087  
1088 **Figure B2: Sediment fraction percentages in Section A - III, recognised by the AI. The visual evaluation included three**  
1089 **classes: gravel – G, sandy gravel – sG, gravelly sand - gS). The fractions of the physical samples are shown as verticals.**





1090  
1091  
1092

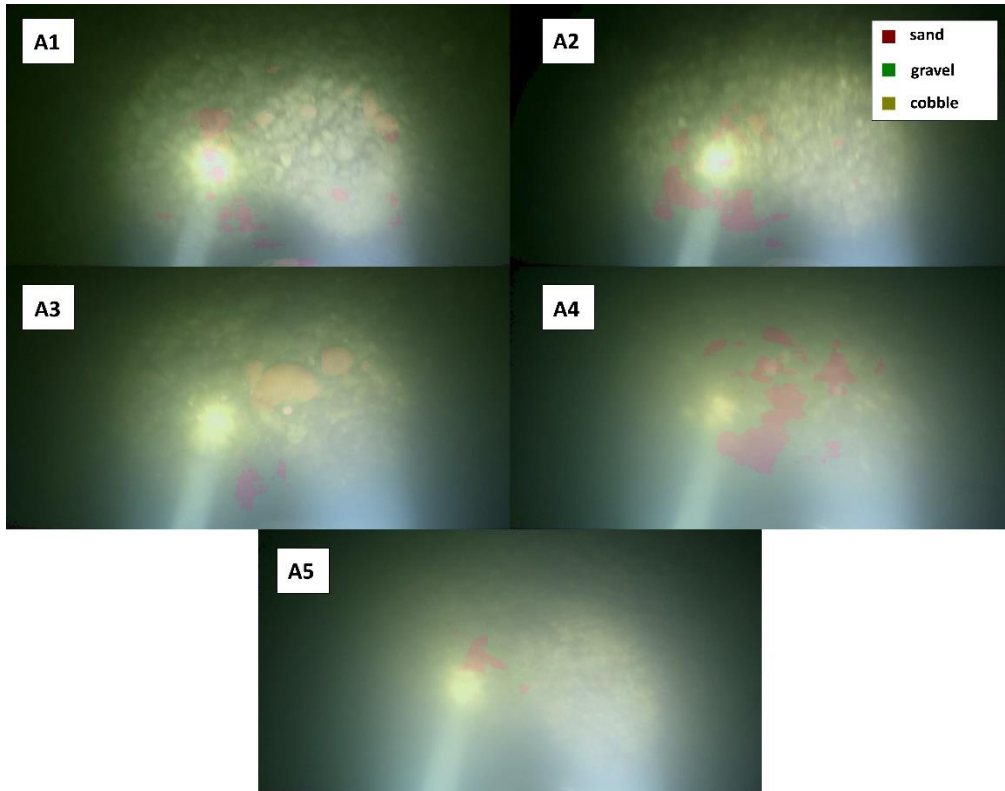
Figure B3: Comparison of sediment fraction % at the sampling locations from the moving-averaged AI detection, conventional sieving and the wavelet-based image processing method. Section A - III.



1093  
1094

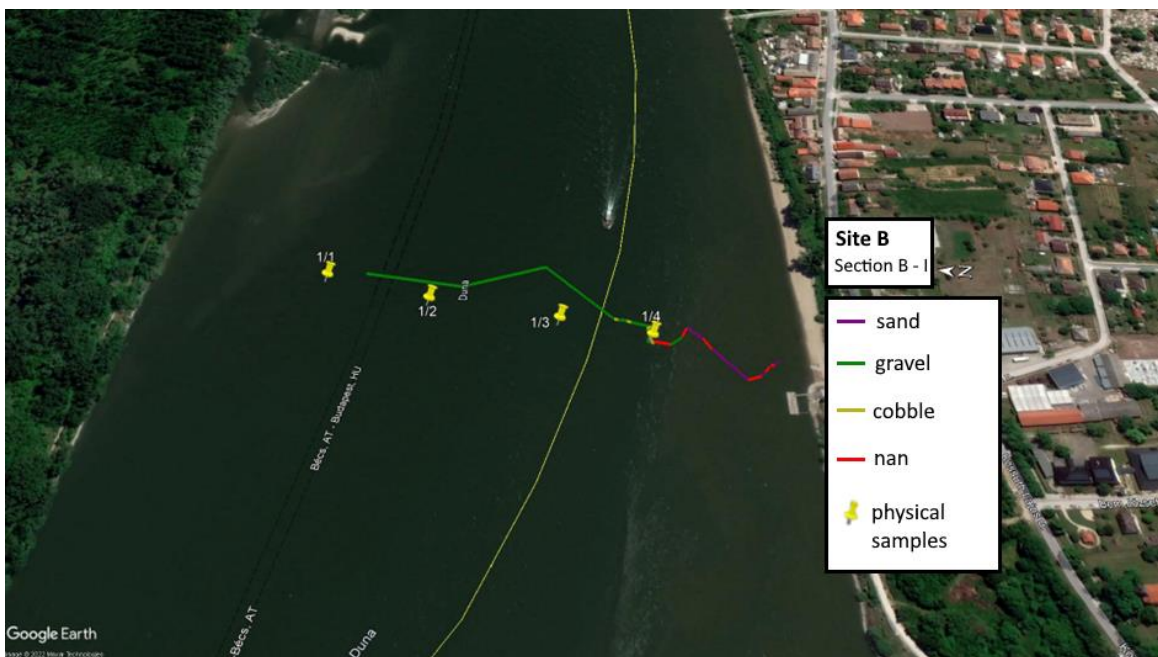
Figure B4: Riverbed video images at the sampling points in Section A - III.

1095

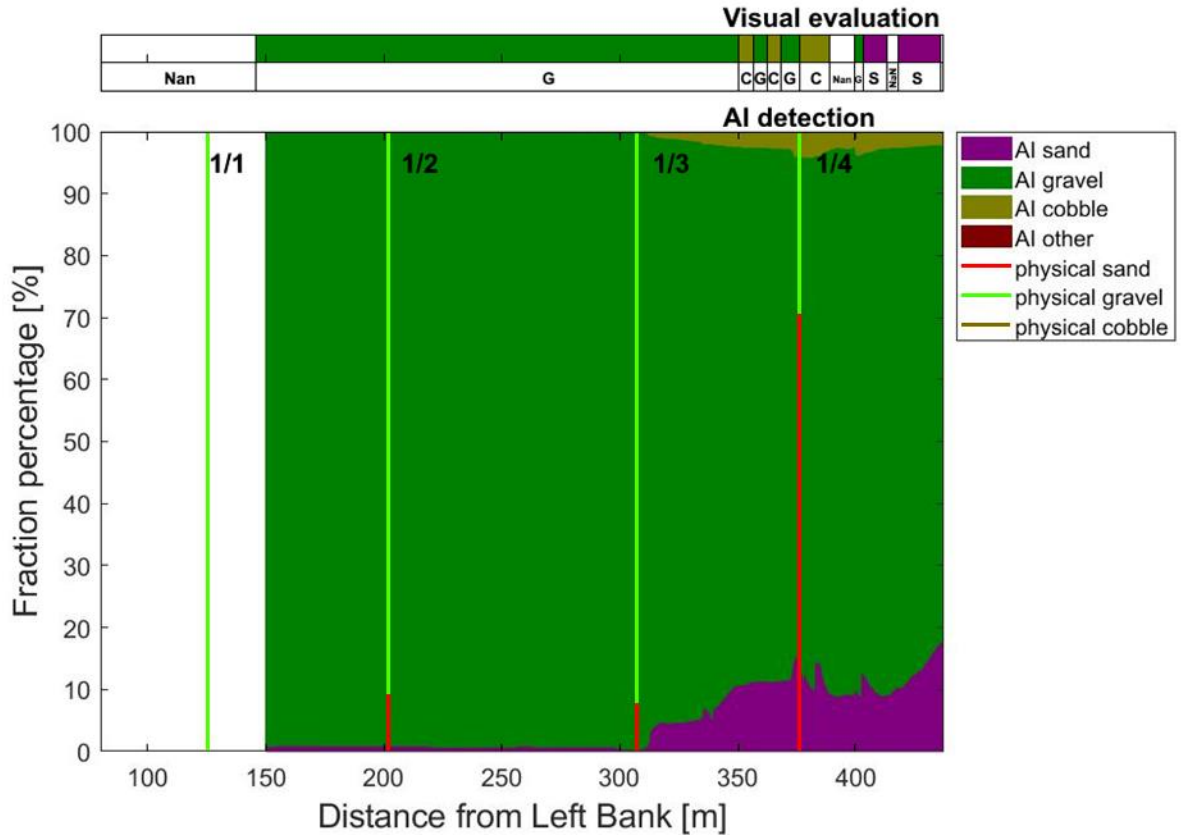


1096  
 1097 **Figure B5: Riverbed video images overlapped with their raw, AI detection result, at the sampling points in Section A -**  
 1098 **III.**  
 1099

1100 **Appendix C Site B – Section B - I**

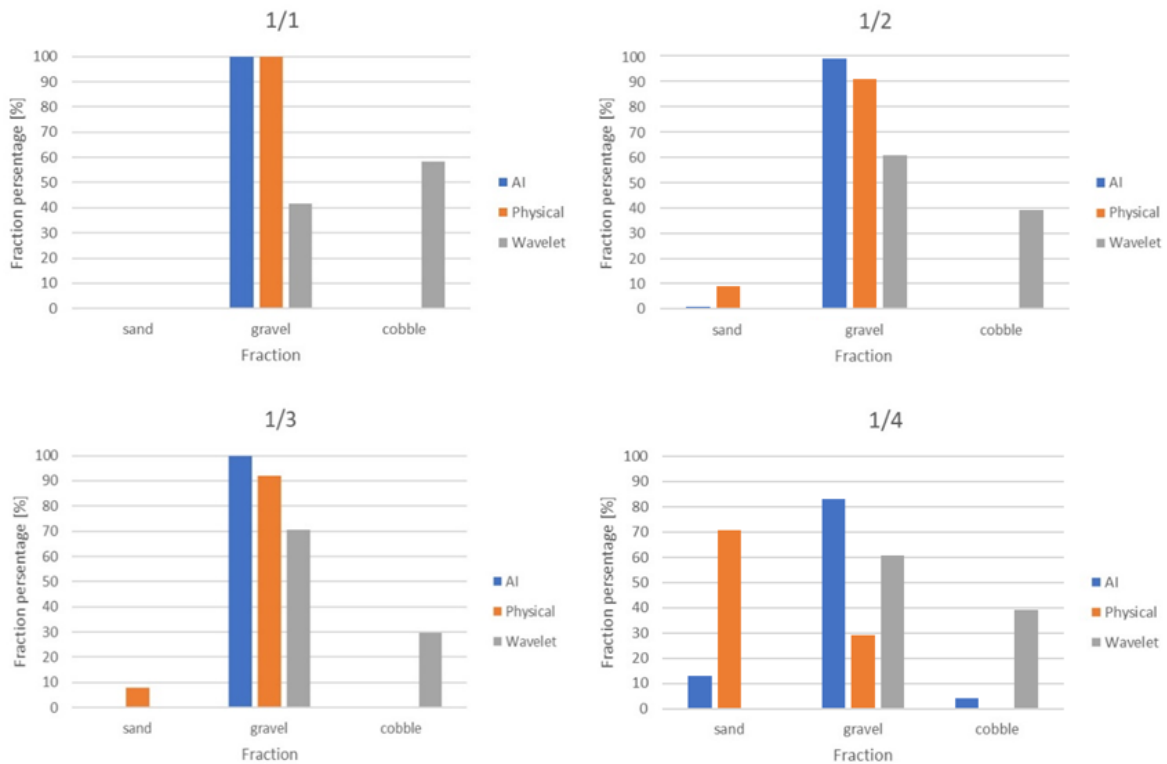


1101  
 1102 **Figure C1: The path of the vessel and camera in Section B - I, Site B. The poly-line is coloured based on the sediment**  
 1103 **seen during visual evaluation of the video. Yellow markers are the locations of physical bed material samplings. (Map**  
 1104 **created with Google Earth Pro)**



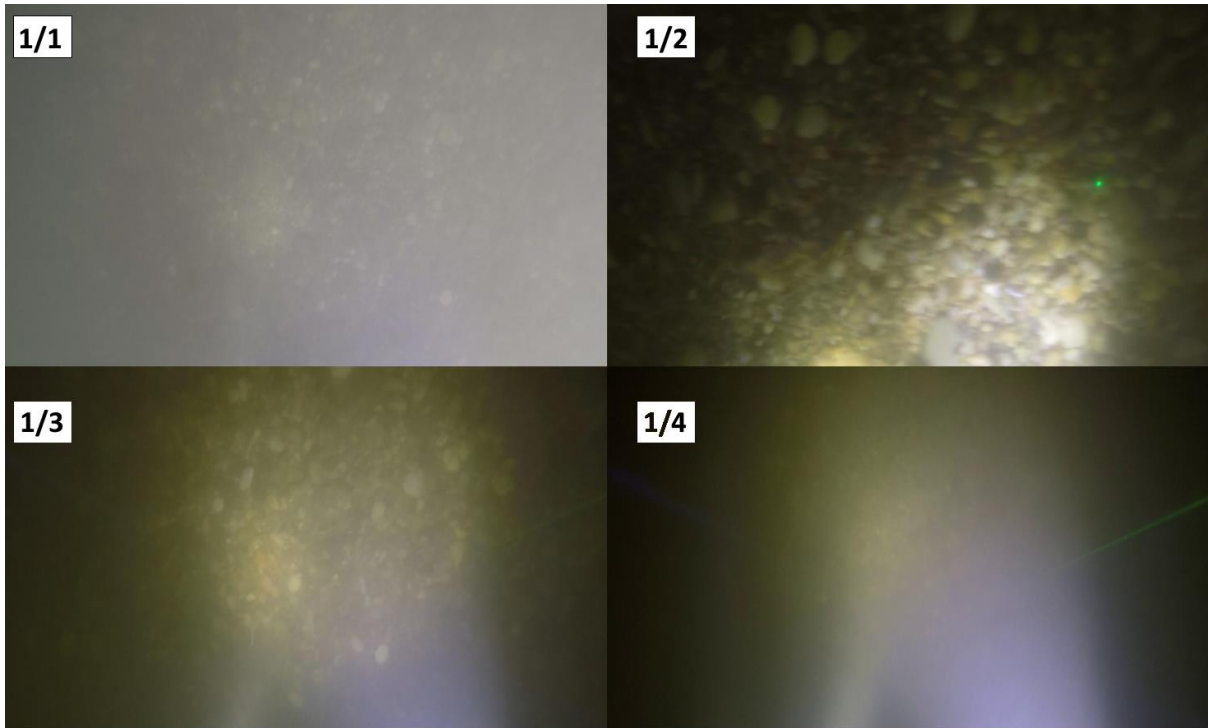
1105  
1106  
1107

Figure C2: Sediment fraction percentages in Section B - I, recognised by the AI. The visual evaluation included two classes: gravel – G, sand – S). The fractions of the physical samples are shown as verticals.



1108  
1109  
1110

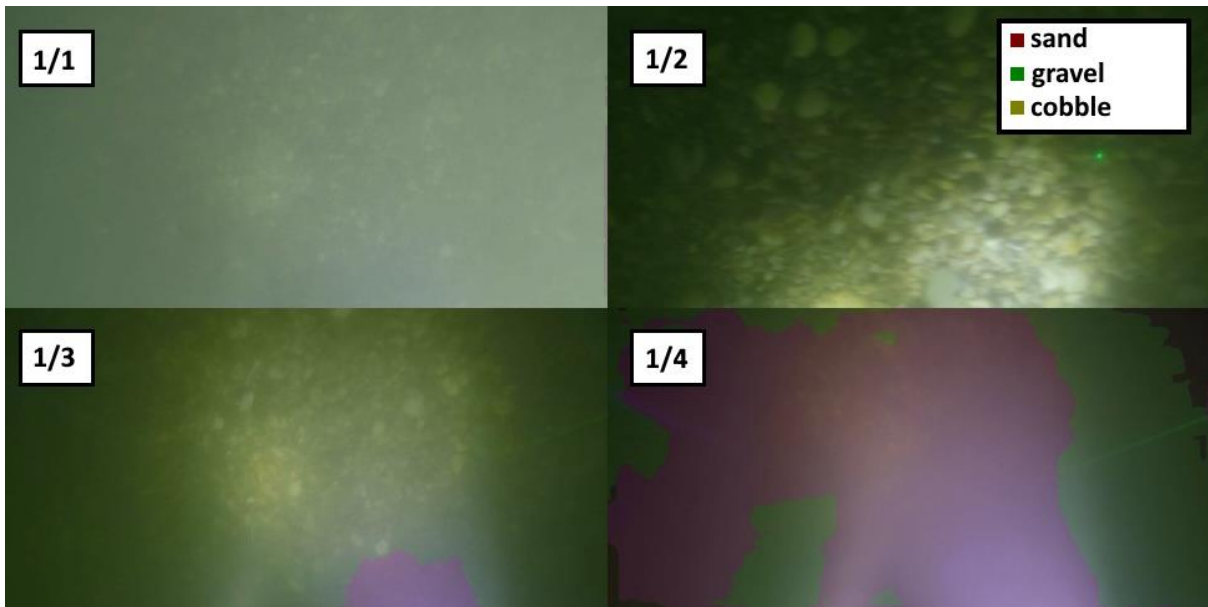
Figure C3: Comparison of sediment fraction % at the sampling locations from the moving-averaged AI detection, conventional sieving and the wavelet-based image processing method. Section B - I.



1111  
1112

Figure C4: Riverbed video images at the sampling points in Section B - I.

1113



1114  
1115  
1116

Figure C5: Riverbed video images overlapped with their raw, AI detection result, at the sampling points in Section B - I.